


Optimized Estimation of Azimuth Cutoff for Retrieval of Significant Wave Height and Wind Speed From Polarimetric Gaofen-3 SAR Wave Mode Data

Zhichao Zheng , Qiushuang Yan , Chenqing Fan , Junmin Meng , Jie Zhang , Tianran Song, and Weifu Sun 

Abstract—This study presents an innovative approach for estimating the azimuth cutoff wavelength (λ_c) using a multipolarization combination technique to enhance the retrieval of significant wave height (SWH) and wind speed (WS) from Gaofen-3 (GF-3) SAR wave mode data. The study identifies distinct advantages of copolarization for low to moderate sea states and cross-polarization for high sea states in the λ_c estimation. Consequently, a suite of dual and quad-polarization combination methods is proposed, with the VV+VH combination demonstrating superior cost-efficiency, reducing the root mean square error (RMSE) of λ_c estimation by around 20% compared with VV polarization. Correlation analysis between λ_c at various polarizations, particularly VV+VH, and factors such as SWH, WS, wind direction, wave direction, and incidence angle, indicates a strong positive relationship with SWH and WS, and a moderate relationship with incidence angle. This insight informs the development of three λ_c -based SWH and WS retrieval models: single linear regression, multiple linear regression (MLR), and Gaussian process regression (GPR). The MLR and GPR models integrate normalized radar cross section (NRCS) and incidence angle to improve retrieval accuracy. The GPR model achieves more accurate estimation of SWH and WS compared with existing λ_c -based algorithms, with an RMSE of 0.485 m for SWH retrieval and 1.390 m/s for WS retrieval. Despite the performance gap with state-of-the-art algorithms, the GPR model offers exceptional cost-effectiveness and surpasses NRCS-based models for WS retrieval without requiring wind direction input.

Index Terms—Azimuth cutoff wavelength (λ_c), Gaofen-3 (GF-3) SAR wave mode (WM), polarization enhancement, significant wave height (SWH), wind speed (WS).

I. INTRODUCTION

SIGNIFICANT wave height (SWH) and wind speed (WS) are two fundamental parameters to characterize the sea state. The accurate detection of SWH and WS on a global scale is critical for a wide range of oceanic, atmospheric, and climate-related applications, as well as ensuring the safety of various human maritime activities such as maritime transportation and offshore engineering [1]. Active microwave remote sensing is presently the primary technique for detecting winds and waves, which is capable of retrieving global SWH and WS under all-weather conditions at all-time from the received electromagnetic waves reflected by the sea surface [2]. Among the commonly used active microwave remote sensing instruments [radar altimeter, wave spectrometer, precipitation radar, scatterometer, and synthetic aperture radar (SAR)], only SAR has the capability to simultaneously observe SWH and WS in high spatial resolution due to its ability to provide fine spatial resolution imagery. The SAR imaging of ocean surface is mainly realized by Bragg resonance scattering, which is affected by three modulation processes [3], [4], [5], [6]. The short waves in Bragg resonance are tilted by long waves (tilt modulation). Their energy is modulated by the hydrodynamic interaction between short waves and long waves (hydrodynamic modulation). Furthermore, the advection of backscattering facet by long wave orbital velocity produces an additional Doppler shift in the return signal and induces an azimuthal displacement of the scattering elements in the SAR image when ocean waves propagate along the SAR azimuth direction as SAR adopts a synthetic aperture imaging (velocity bunching). Tilt modulation and hydrodynamic modulation only affect the strength distribution in SAR imaging, whereas velocity bunching can result in image blurring and make waves with wavelengths less than a certain threshold unobservable by SAR [6]. This problem is generally called the azimuth cutoff phenomenon, and the critical wavelength is known as the azimuth cutoff wavelength (λ_c) [7].

There are many algorithms that allow estimation of SWH from SAR. The initial algorithms, such as Max Planck Institute algorithm [6], [8], cross-spectral algorithm [9], semiparametric retrieval algorithm [10], partition rescaling and shift algorithm [11], and parameterized first-guess spectrum method [12], were

Manuscript received 6 December 2023; revised 21 February 2024 and 18 April 2024; accepted 21 May 2024. Date of publication 27 May 2024; date of current version 14 June 2024. This work was supported in part by the National Key Research and Development Program of China under Grant 2021YFC3101102, and in part by the National Natural Science Foundation of China (NSFC) under Grant 61931025 and Grant 42206178. (Corresponding author: Qiushuang Yan.)

Zhichao Zheng, Qiushuang Yan, and Tianran Song are with the College of Oceanography and Space Informatics, China University of Petroleum, Qingdao 266580, China (e-mail: 577952978@qq.com; yanqiushuang@upc.edu.cn; s20160002@s.upc.edu.cn).

Chenqing Fan, Junmin Meng, Jie Zhang, and Weifu Sun are with the First Institute of Oceanography, Ministry of Natural Resources, Qingdao 266061, China (e-mail: fanchenqing@fio.org.cn; mengjm@fio.org.cn; zhangjie@upc.edu.cn; sunweifu@fio.org.cn).

Digital Object Identifier 10.1109/JSTARS.2024.3405736

developed based on the classical nonlinear SAR-wave imaging relationship derived from the modulation theory of SAR ocean imaging. They were designed to first retrieve directional wave spectra, and then compute SWH via spectral integration. However, it is problematic to derive accurate and complete directional wave spectrum from SAR with these algorithms due to the azimuth cutoff effects and the lack of understanding of hydrodynamic modulation process [13]. Empirically estimating SWH from SAR has become an alternative approach. The classical attempts were a series of CWAVE models that established a relationship between SWH and two image-based variables, namely, the normalized radar cross section (NRCS) and the image variance (cvar), as well as 20 spectral parameters extracted from SAR image spectrum using a set of orthogonal functions [14], [15], [16], [17]. In addition, various models were developed from the dependence of SWH on λ_c , on its own or combined with one or several of the variables such as NRCS, cvar, skewness, kurtosis, peak wavelength, peak wave direction, and incidence angle (θ) [16], [18], [19], [20], [21], [22], [23], [24]. Recently, several machine learning and deep learning models have been developed to predict SWH from SAR using some or all of the features mentioned above [24], [25], [26], [27], [28], [29]. The early investigations were primarily focused on predicting SWH solely from single-polarization SAR (mostly VV) [14], [15], [16], [18], [19], [20], [21], [24], [27], [28]. Then, several studies showed that cross-polarization (HV and VH) information can help to improve SWH retrieval performance [30]. Recent studies have shifted their focus toward exploring the enhancement of combination of multiple polarizations [17], [22], [23], [25], [26], [29]. The SAR SWH retrieval entails a multitude of features, and the inclusion of multipolarization information leads to a multiplication in their number. The utilization of so many features will make the SAR SWH retrieval algorithms more intricate, which can improve the retrieval accuracy while also making the retrieval algorithms susceptible to overfitting.

Spaceborne SAR has the capability to measure sea surface winds at a spatial resolution of meters, which is particularly crucial in coastal zones where the surface wind field often exhibits significant spatial variability due to coastal topography and anthropogenic structures (e.g., [31]). This triggers the development of wind retrieval techniques based on SAR data. The typical methodology for deriving wind field from SAR is to apply a copolarization (mostly VV) empirical geophysical model function (GMF) to the corresponding calibrated SAR NRCS images with wind direction obtained from external sources or wind streaks visible in SAR imagery (e.g., [32], [33], and [34]). Basically, the HH SAR NRCS are converted to VV NRCS by using polarization ratio models (e.g., [35]). The effectiveness of such a technique is limited by the difficulty in accurately determining wind direction [36]. Moreover, the copolarization NRCS displays a saturation trend at WSs as low as 16 m/s for incidence angles below 35° , thereby constraining the accuracy of high wind retrieval [37]. These issues are also present in the machine learning models developed for SAR WS retrieval based on the copolarization NRCS measurements [38]. To address these issues, WS retrieval techniques using cross-polarization GMFs have been proposed (e.g., [39], [40], and [41]). The

cross-polarization NRCS shows increased sensitivity to high WSs and delayed signal saturation (if exist), and its dependence on azimuth angle with respect to the wind direction is negligible in comparison with the WS dependence [39]. Retrieving WS from cross-polarization SAR NRCS is a straightforward process, followed by obtaining wind direction from copolarization SAR NRCS [41]. However, the cross-polarization SAR images have low signal-noise-ratio (SNR) at low-to-moderate winds, which hinders its ability to achieve high-accuracy retrieval of such winds [39].

Azimuth cut-off wavelength can play a significant role in both SWH and WS retrieval. Recently, we compared the performance of SWH retrieval algorithms using different SAR features as input, and found that the utilization of λ_c alone or in combination with a selected few parameters can yield estimations of fairly high accuracy [25], [42]. The λ_c -based SWH retrieval algorithms exhibit a superior level of cost-effectiveness in comparison to others. In the field of SAR WS retrieval, NRCS is a very important and classic parameter. In addition to NRCS, λ_c is found to be another SAR parameter that exhibits a strong correlation with WS (e.g., [23], [42], and [43]). It has been used to retrieve WS through linear correlations for WSs less than 25 m/s [42]. And studies have pointed out that the λ_c -based technique has a certain potential for high WS retrieval [43]. Furthermore, this technique requires neither calibration of the SAR data nor any a priori knowledge on wind direction [43]. Therefore, the λ_c -based technique is expected to serve as an effective supplement to the NRCS-based technique for wind retrieval, and it has recently gained more attention [23], [43].

The effectiveness of the λ_c -based algorithms in retrieving SWH and WS from SAR is heavily reliant on the accuracy of λ_c estimation, which is affected by many factors. The λ_c estimation primarily relies on the velocity bunching modulation, intrinsic scene coherence time, and ocean wave spectrum [23]. Furthermore, several studies have demonstrated that it is also affected by SAR pixel spacing, polarization, and incidence angle [23], [43], [44]. Corcione et al. [43] analyzed and optimized the SAR pixel spacing, the size of SAR image boxes, and the texture of SAR ocean scenes in terms of λ_c estimation. Li et al. [44] investigated the dependence of the λ_c estimation on polarization and incidence angle, revealing that the λ_c values estimated under VH polarization are generally larger than the HH ones, the latter already being larger than the VV ones, and this trend increases with the incidence angle. Bao et al. [23] conducted an analysis of the correlation between λ_c and SWH and WS under different polarization bases, and found that the λ_c estimated under the elliptical polarization bases exhibits a stronger correlation with SWH and WS than that under H-V linear, circular, and linear rotated polarization bases. Pramudya et al. [22] proposed a novel strategy to estimate SWH, which uses the combination of the spectra of VV and VH polarization SAR images to optimize the estimation of λ_c , and thus the estimation of SWH. Given the aforementioned, in conjunction with selecting appropriate values for the SAR parameters that influence the estimation of λ_c , the combined use of multiple polarizations can improve the accuracy of estimating λ_c . However, how to set the parameters and how to fully utilize the SAR polarimetry information to

achieve optimal estimation of λ_c , and therefore, optimal estimation of SWH and WS, are still topics of debate. The technique for estimating λ_c should undergo a comprehensive optimization and assessment.

In this article, we propose an optimized approach for λ_c estimation based on the quad-polarization Gaofen-3 (GF-3) SAR wave mode (WM) data, and evaluate its performance by comparing it with the simulated λ_c values from the 2-D wave spectrum provided by the European Centre for Medium Range Weather Forecasts (ECMWF) fifth generation reanalysis (ERA5). The effects of the optimization on the correlation between λ_c and SWH (WS), as well as on the retrieval of SWH and WS are subsequently evaluated.

The rest of this article is organized as follows. Section II introduces the data and methods. In Section III, the optimized strategy for λ_c estimation is proposed and assessed. Section IV analyzes the impact of the optimization on the correlation between λ_c and SWH and WS. In Section V, the enhancement of the optimized λ_c estimation on the retrieval of SWH and WS from GF-3 SAR is verified. Section VI discusses the impact of the distribution of sea states in the dataset on the accuracy of retrieval algorithm. Finally, Section VII concludes this article.

II. DATA AND METHODS

This study utilizes the GF-3 SAR WM data as well as the ocean wave spectra and wind and wave parameters data from ECMWF ERA5. The ERA5 ocean wave spectra are employed to provide λ_c simulations as references for evaluating the performance of λ_c estimation from quad-polarization GF-3 SAR WM data. The ERA5 wave and wind parameters serve as standard references for quantifying the dependence of λ_c on ocean surface wind and wave characteristics. Detailed descriptions of all datasets are provided below.

A. GF-3 WM Data

The GF-3 satellite, which was successfully launched in August 2016, is equipped with a C-band SAR sensor operating at a radar frequency of 5.3 GHz. It remains operational in orbit up to this point. Among its 12 working modes, the WM is specifically designed for ocean observation. The in-orbit external calibration experiment indicates the worst noise equal sigma zero (NESZ) ranges from -20 dB to -22 dB for different GF-3 SAR working modes. For WM images, when the resolution is less than 10 m, the worst NESZ is -20 dB [45]. In WM, GF-3 SAR acquires one small image (referred to as imagette) covering an area of approximately $5 \text{ km} \times 5 \text{ km}$ while maintaining a nominal spatial resolution of up to 4 m every 50 km along the flight direction, and it offers quad-polarization (HH, HV, VH, and VV) measurements at various incidence angles of 20° – 50° .

The GF-3 WM L1A single-look complex (SLC) imagette products for the period of 2017 to 2018 were collected. After excluding data with excessive power saturation and discarding imagettes contaminated by sea ice, land/island, or those that failed the homogeneity check, a total of 11 163 imagettes

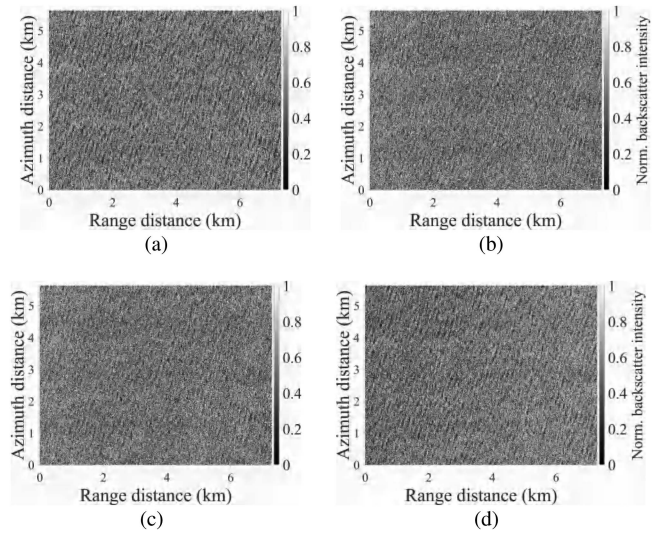


Fig. 1. Case of GF-3 WM imagettes acquired on 7 February, 2017 at 18:17:16 UTC. The images are normalized by the min-max method. (a) HH image, (b) HV image, (c) VH image, and (d) VV image.

were selected for the following experiment. The homogeneity check was conducted using the methodology proposed by Stellenfleth et al. [46]. Fig. 1 presents a typical example of the quad-polarization GF-3 WM imagettes. The display of the four polarized images exhibits distinct variations, yet all demonstrate a clear wavy structure, albeit with slightly blurred patterns in the cross-polarization images. The GF-3 SAR imagettes undergo radiometric calibration to convert the intensity values of the imagettes into their corresponding NRCS. The GF-3 NRCS values can be obtained by the following:

$$\sigma^0 = 10 \log_{10} \left[DN \times \left(\frac{qv}{32767} \right)^2 \right] - K \quad (1)$$

where σ^0 is the NRCS in dB, DN denotes the imagette intensity that satisfies $DN^2 = P^2 + Q^2$, where P and Q are, respectively, the real and imaginary parts of the imagette, qv and K are, respectively, the maximum qualified value and calibration coefficient of the imagette, which are stored in the product annotation file according to polarizations. However, the majority of official GF-3 WM products do not offer the quad-polarization K values. Therefore, we conducted an ocean recalibration to re-estimate the K values for the quad-polarization GF-3 WM imagettes. The detailed description of the recalibration process can be found in [25]. Then the quad-polarization NRCS values were estimated from the corresponding GF-3 SAR SLC data using the recalibration constants.

Fig. 2 illustrates the process of estimating λ_c from a SLC imagette of GF-3 WM, with detailed descriptions of the key steps provided below.

- 1) The slant-range SAR complex imagette is converted into a ground-range imagette.
- 2) The ground-range complex imagette undergoes Fourier transform and range-averaging to obtain the azimuth wave number spectrum.

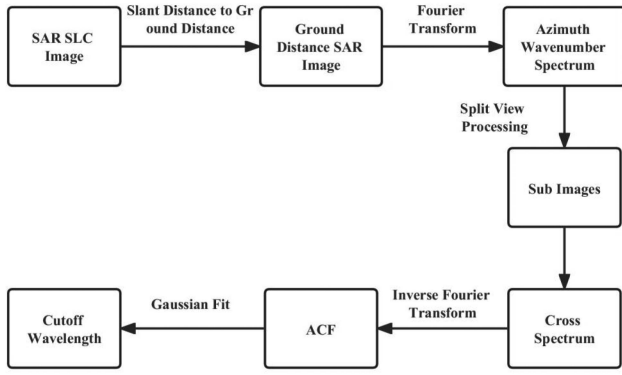
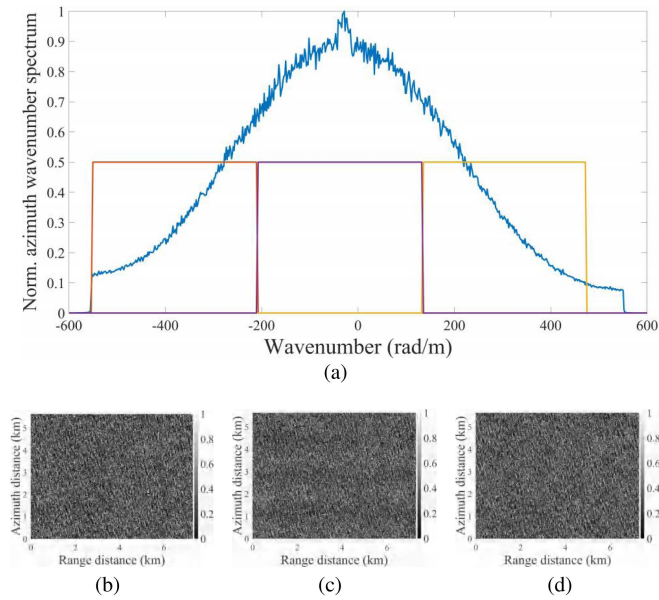

 Fig. 2. Flowchart for the estimation of λ_c .


Fig. 3. (a) Plot of azimuth wave number spectrum and three gate functions. (b) Normalized subintensity image 1. (c) Normalized subintensity image 2. (d) Normalized subintensity image 3.

- 3) The azimuth wave number spectrum is convolved with three gate functions to derive three subazimuth wave number spectra, which are then subjected to inverse Fourier transform to obtain three subimages (see Fig. 3).
- 4) The three subimages undergoes Fourier transform to obtain three subintensity spectra.
- 5) The cross spectrum is calculated from the three subintensity spectra using the following:

$$\bar{\Phi}_k = \frac{\hat{I}_k^1 (\hat{I}_k^2)^* + \hat{I}_k^2 (\hat{I}_k^3)^*}{2} \quad (2)$$

where $\bar{\Phi}_k$ represents the cross spectrum, \hat{I}_k^1 , \hat{I}_k^2 , and \hat{I}_k^3 are the intensity spectra of subimages 1, 2, and 3, respectively, and $*$ denotes taking the complex conjugate.

- 6) The auto-correlation function (ACF) is computed by applying an inverse Fourier transform to the real part of the cross spectrum.

- 7) The λ_c is estimated by fitting a Gaussian function to the ACF, which is stated as follows:

$$C(x) = \exp\left(-\left(\frac{\pi x}{\lambda_c}\right)^2\right) \quad (3)$$

where $C(x)$ is the Gaussian function and x is the azimuth spatial distance.

Previous studies (e.g., [42] and [43]) have demonstrated that the pixel spacing exerts a direct influence on the SAR estimation of λ_c , with larger pixel spacing resulting in an increase in its value. However, there is almost no specific analysis of the impact of pixel spacing on the accuracy of λ_c estimation. The impact of pixel spacing on the accuracy of λ_c estimation is investigated here by comparing the estimated λ_c from GF-3 SAR imagerettes at different pixel spacings, ranging from the nominal 4 m spatial resolution to 24 m in 2 m steps, with the simulations derived from ERA5 wave spectra.

Corcione et al. [43] demonstrated that median filter can be integrated into λ_c estimation process because it can mitigate the dependence of ACF fits on pixel spacing and enhance the reliability of λ_c estimation by removing the speckle noise peaks. Experimental evidence suggests that the utilization of the conventional fixed window median filter, specifically employing an 11-pixel window, can optimize the λ_c estimation at low pixel spacing. However, as the pixel spacing increases, there is a significant reduction in the number of sample points of the ACF, leading to abnormally small values of λ_c when using the conventional 11-pixel median filter. To address this limitation, we employ an adaptive median filter that dynamically adjusts the size of the filtering window based on variations in pixel spacing. The number of pixels of the adaptive median filter window, N_p , can be determined by the following in [43]:

$$N_p = \text{int} \left[\frac{\text{WS}^{(m)}}{\Delta x} \right] + 1 \quad (4)$$

where $\text{WS}^{(m)}$ is the window size of the adaptive median filter in meters, Δx represents the pixel spacing, and int means round down to the nearest integer. The specific implementation requires an odd value for N_p . If the calculated result of N_p is even, it should be decremented by 1. The window size of the adaptive median filter is determined as 80 m after conducting multiple experiments and tests.

The statistics metrics of root mean square error (RMSE), mean error (Bias), correlation coefficient (Corr), and scatter index (SI) are used to assess the accuracy of λ_c estimated from quad-polarization GF-3 WM imagerettes in comparison with the λ_c simulated from ERA5 directional wave spectra. Fig. 4 illustrates the error metrics of λ_c estimated from GF-3 SAR imagerettes with and without median filter, showcasing their dependence on pixel spacing ranging from 4 to 22 m. The results at the pixel spacing of 24 m are not presented due to an insufficient number of sample points in the ACF resulting in a significant abnormality in estimating λ_c . As shown in Fig. 4, the RMSE and Bias of the SAR-estimated λ_c exhibit a decreasing trend when the pixel spacing is below approximately 12 m, whereas an increasing trend is observed at larger pixel spacings. That is

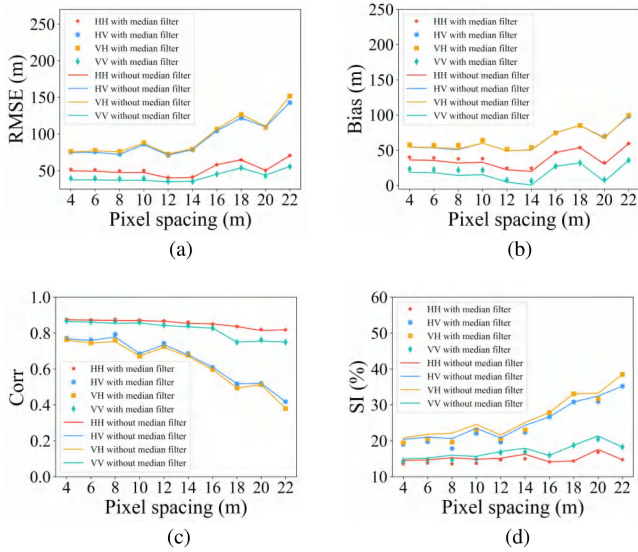


Fig. 4. (a) RMSE, (b) Bias, (c) Corr, and (d) SI of GF-3 SAR estimated λ_c relative to ERA5 simulated λ_c at polarizations of HH, HV, VH, and VV with and without median filter as functions of pixel spacing.

to say, the RMSE and Bias both reach their minimum values at a pixel spacing of approximately 12 m. Moreover, despite a decreasing trend in Corr and an increasing trend in SI with the increase of pixel spacing, the variations of Corr and SI are rather small at pixel spacings lower than about 12 m. These scenarios arise across all the four polarizations of HH, HV, VH, and VV. However, the impact of pixel spacing on λ_c estimation is considerably more pronounced in cross-polarizations such as HV and VH than in copolarizations such as HH and VV.

The utilization of the adaptive median filter, which results in slightly lower RMSE and Bias, can marginally enhance the estimation of λ_c . And this enhancement is relatively obvious at lower pixel spacings. Given the above, it is more advantageous to estimate λ_c from GF-3 SAR WM imagnettes at a pixel spacing of 12 m. And at this pixel spacing, the adaptive median filter exhibits certain optimization effects. In the following experiment, a 12-m pixel spacing and the adaptive median filter are adopted to estimate λ_c from GF-3 SAR imagnettes.

Fig. 5 (Left) shows the real parts of the image cross spectra of the imagnette presented in Fig. 1 for the four polarization channels of HH, HV, VH, and VV. Fig. 5 (Right) shows the corresponding estimation of λ_c by fitting (3) to the ACF. As shown, the peak wavelength is around 180 m. The copolarization spectra (HH and VV) exhibit lower levels of noise compared with the cross-polarization spectra (HV and VH). This is probably because the cross-polarization imagery is more sensitive to oceanic physical phenomena, such as wave breaking and currents [47]. The spectral amplitude of HH polarization is higher than that of VV, whereas the latter exceeds the cross-polarization spectra. This may be partially attributed to the variation in real aperture radar (RAR) modulation transfer function (MTF), which is highest at HH polarization and lowest at cross-polarizations [44]. Similarly, the HH λ_c estimate is slightly bigger than the VV estimate due to the larger HH RAR MTF. However, the cross-polarization λ_c estimates are even greater than the HH one,

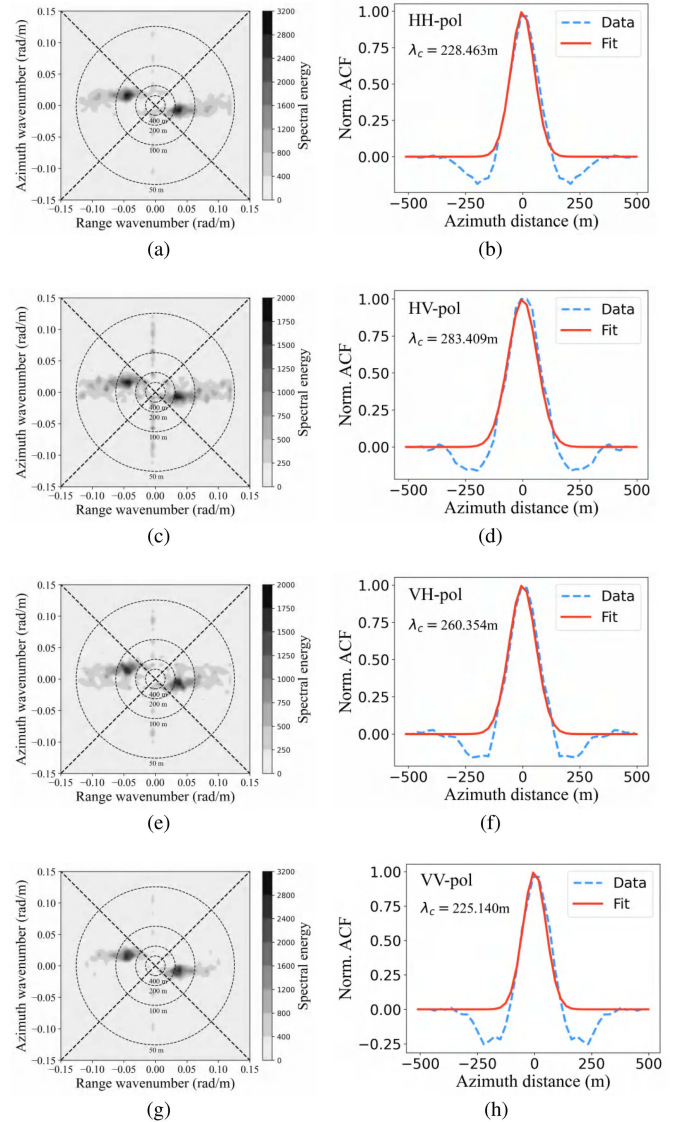


Fig. 5. (Left) Real part of SAR image cross spectra of the GF-3 WM imagnette depicted in Fig. 1 for the four polarization channels of (a) HH, (c) HV, (e) VH, and (g) VV. (Right) Corresponding azimuth cutoff estimation for the four polarization channels of (b) HH, (d) HV, (f) VH, and (h) VV.

despite the significantly smaller values for cross-polarization RAR MTFs. This may be attributed to the prevalence of smearing effects in the HV (VH) imagnettes, which are likely associated with shorter lifetimes of HV (VH) scatters [44]. These findings are essentially in line with those reported in [44].

B. ERA5 Data

ERA5 is the fifth generation reanalysis of ECMWF, which combines model data with observations from around the world to provide hourly estimates for a large number of atmospheric, ocean-wave, and land-surface quantities [39]. In this study, the products of global-scale ERA5 directional wave spectra and the associated sea state parameters, including the significant height of combined wind waves and swell (i.e., SWH), the mean wave direction (φ_{wave}), the 10 m u-component of neutral wind (u_{10}),

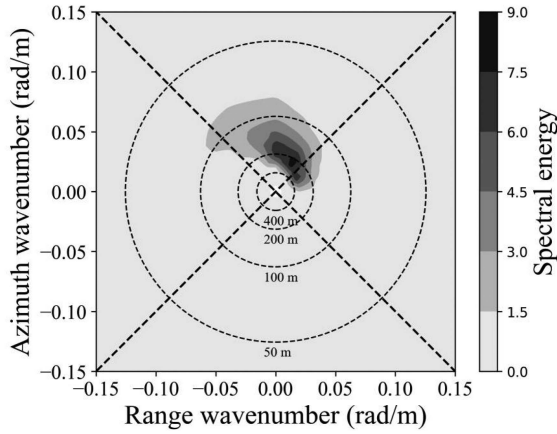


Fig. 6. Plot of the ERA5 directional wave spectrum on 7 February, 2017 at 18:00:00 UTC closest in space and time to the imagette presented in Fig. 1.

and the 10 m v-component of neutral wind (v_{10}), provided by the ERA5 hourly data on single levels for the period from 2017 to 2018 are collected. The wave spectra, SWH and φ_{wave} data are gridded onto a regular latitude-longitude grid with a resolution of 0.5° , whereas the u_{10} and v_{10} data are gridded with a spacing of 0.25° . The WS values are obtained by computing the square root of the sum of u_{10} squared and v_{10} squared. The wind direction (φ_{wind}) can be obtained by taking the arctangent of u_{10}/v_{10} . According to Rivas and Stoffelen [48], the ERA5 shows some important persistent biases in several regions around the world. Subsequently, Zhai et al. [49] validated the ERA5 wind and wave data through comparison with the buoy data, revealing that the error of ERA5 WS is less than 1 m/s and that of ERA5 SWH is less than 0.3 m, thus demonstrating the high reliability of ERA5 reanalysis data.

ERA5 directional wave spectra are generated by the wave model. Each wave spectrum consists of components distributed in a frequency-direction grid, with 30 wave frequencies ranging from 0.0345 to 0.5478 Hz and 24 circular directions evenly spread with an interval of 15° . In this study, the directional frequency spectrum $S(f, \phi)$ should be transformed into the wave number spectrum $S(k, \phi)$. According to [50], $S(k, \phi)$ is expressed in terms of $S(f, \phi)$ as follows:

$$S(k, \phi) = S(f, \phi) \frac{df}{dk} = \frac{S(f, \phi)g}{8\pi^2 f} \left[\tanh(kh) + \frac{kh}{\cosh^2(kh)} \right] \quad (5)$$

where k is the wave number, f is the wave frequency, ϕ is the wave propagation direction, $g = 9.8 \text{ m/s}^2$ is the gravitational acceleration, and h is the water depth. Here, h is assumed to be infinite, which makes the value in the brackets equal to 1. Fig. 6 shows the ERA5 directional wave spectrum that is spatiotemporal closest to the imagette presented in Fig. 1. By comparing the ERA5 spectrum in Fig. 6 with the corresponding SAR cross-spectrum in Fig. 5, it is evident that SAR exhibits a loss of small-scale wave information in the azimuthal direction, referred to as the azimuth cutoff phenomenon. From the ERA5 wave number spectra, the λ_c simulations can be obtained based

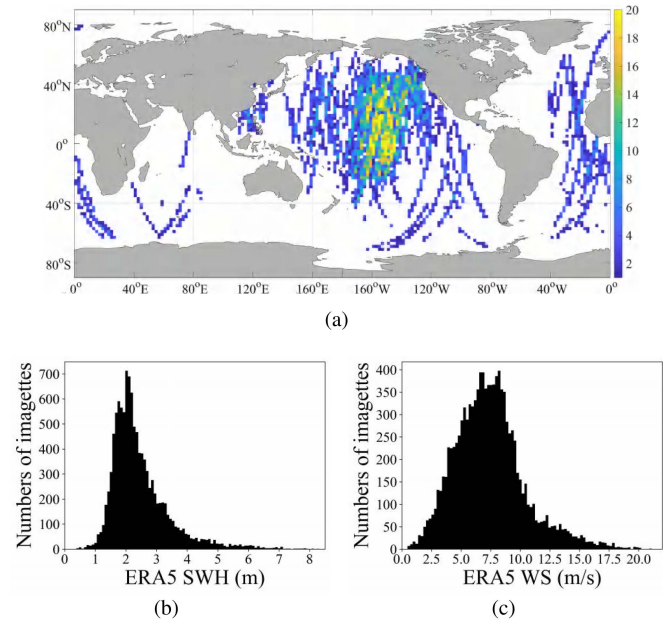


Fig. 7. Distribution of GF-3 WM imagettes matched with ERA5 data. (a) Locations of GF-3 WM acquisitions on a $2^\circ \times 2^\circ$ grid. (b) Histogram of ERA5 SWH. (c) Histogram of ERA5 WS.

on the following [19]:

$$\lambda_c = \pi\beta \sqrt{\int |T_k^v|^2 S(k, \phi) d\phi dk} \quad (6)$$

$$\beta = \frac{R}{V} \quad (7)$$

$$T_k^v = -\omega \left(\sin \theta \frac{k_r}{|k|} + i \cos \theta \right) \quad (8)$$

where β the slant range (R) to velocity (V) ratio of the SAR platform, T_k^v is the range velocity transfer function, ω is the angular frequency, θ is the incidence angle, and k_r is the component of the wave number k in the radar range direction. The values of R , V , and θ can be obtained from the GF-3 annotation file.

C. Collocations

Each GF-3 imagette is collocated with the ERA5 wave spectrum at a temporal interval of 30 min and a spatial interval of 0.25° . These intermediate collocations are then further matched with the time/space interpolated ERA5 wave and wind parameters. This collocation procedure results in approximately 11 163 matched pairs of GF-3 SAR - ERA5 spectrum - ERA5 wave and wind parameters. Fig. 7(a) displays the locations of GF-3 WM acquisitions in the matched dataset. Fig. 7(b) shows the histogram of matched ERA5 SWH. Fig. 7(c) presents the histogram of matched ERA5 WS. The matched points are evenly distributed across the global ocean, with the majority located in the Pacific Ocean. The collocated ERA5 SWH ranges roughly from 0.3 to 8.5 m, and the WSs vary from 0 to 20 m/s. The majority of the matched data is distributed within moderate sea states, whereas limited data are available for high sea states where the SWH exceeds 4 m or the WS is larger than 15 m/s.

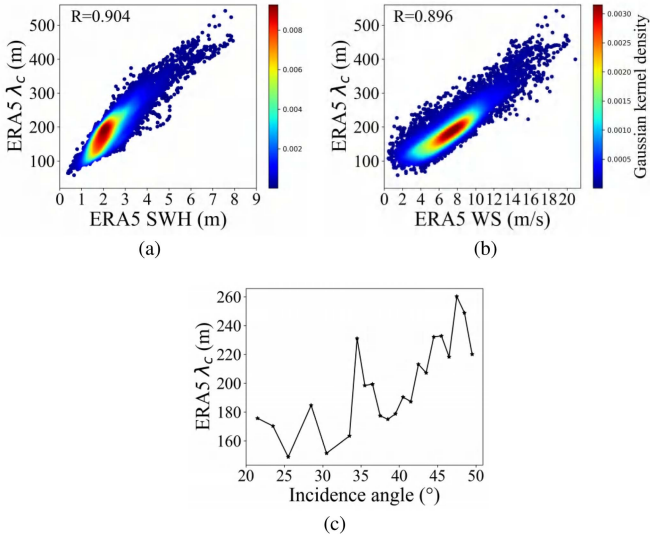


Fig. 8. ERA5 λ_c simulations as functions of (a) SWH, (b) WS, and (c) incidence angle. Colors in (a) and (b) represent the density of data points based on Gaussian kernel estimation. A higher value indicates a greater concentration of data.

To investigate the impact of sea states on λ_c , we partition the collocated dataset into two subsets based on the method outlined in [51]. One is distributed under swell-dominated sea states (10 714 points) and the other is under wind wave-dominated sea states (449 points). The criteria for distinguishing sea states are provided in Appendix. The example depicted in Fig. 1 represents a case under swell-dominated sea states.

The λ_c simulations corresponding to the GF-3 SAR imagettes can be derived from the collocated ERA5 wave spectra. Fig. 8 illustrates the dependences of the simulated λ_c on SWH, WS, and incidence angle. As shown, the simulated λ_c generally exhibits an increasing trend with increasing SWH and WS. There exists a strong correlation between simulated λ_c and SWH as well as WS with Corrs of approximately 0.9. The impact of incidence angle on simulated λ_c is weak at lower angles ($< \sim 33^\circ$), whereas at higher angles, there is a significant increase in simulated λ_c with increasing incidence angle.

III. OPTIMIZED ESTIMATION OF λ_c THROUGH MULTIPOLARIZATION COMBINATION

In this section, the influence of polarization on λ_c estimation is analyzed in detail, and optimized λ_c estimation methods are tested for four types of dual-polarization combination and four types of quad-polarization combination.

A. Effects of Polarization

The λ_c estimation from GF-3 SAR displays noticeable polarization sensitivity. To emphasize the differing sensitivity to polarization, the λ_c estimates from one polarization are displayed relative to another, as depicted in Fig. 9. Fig. 9 also shows the root mean square displacement (RMSD), mean displacement (MD), and Corr (R) of the λ_c estimates from one polarization relative to those from another. As found, the VV λ_c estimates tend to

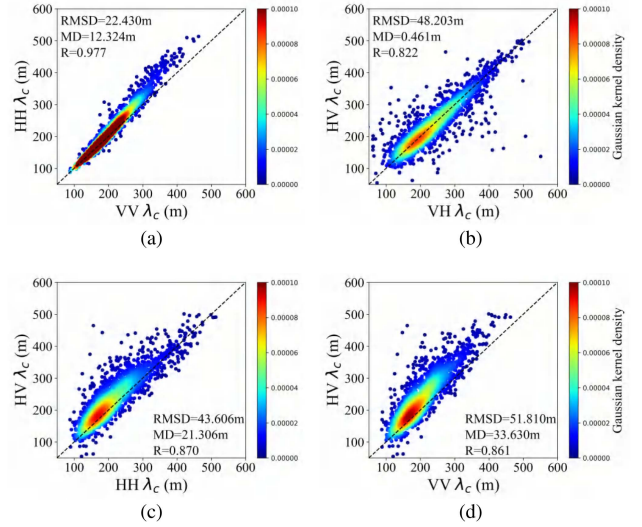


Fig. 9. Comparison of λ_c estimations under different polarizations. (a) HH λ_c versus VV λ_c . (b) HV λ_c versus VH λ_c . (c) HV λ_c versus HH λ_c . (d) HV λ_c versus VV λ_c . Dashed lines represent the one-to-one diagonal. Color denotes data density. The RMSD, MD, and R of the λ_c estimates from one polarization (Y-axis) relative to those from another polarization (X-axis) are labeled in each panel.

be lower than the HH estimates, with a widening disparity as λ_c increases. As well, the VV estimates are generally smaller than the HV ones, and the deviation increases with λ_c . Generally, the HV estimates are even larger than the HH estimates, though they are very close to each other at higher λ_c . The VH estimates are basically at the same level as the HV estimates. In summary, the HV/VH estimates are generally the largest, followed by the HH estimates, while the VV estimates are the smallest. This is consistent with the results of [46]. The largest HV/VH estimates result from the smearing effects caused by breaking events, which are the dominant contributor to cross-polarization backscatter. The larger HH estimates, in comparison to VV ones, are attributed to the larger RAR MTF. The smearing effects also contribute to the increase in HH cutoff values, as breaking events play a significant role in HH backscatter [52].

Fig. 10 shows comparison of GF-3 SAR λ_c estimations with ERA5 λ_c simulations for the four polarizations of HH, HV, VH, and VV. It can be seen that all four polarizations exhibit positive biases, suggesting a general tendency to overestimate λ_c . Among them, the VV polarization shows the lowest bias (21.124 m) and the smallest RMSE (43.853 m), indicating superior performance in estimating λ_c . Following that is the HH polarization, with a bias of 33.448 m and an RMSE of 48.989 m. The cross-polarizations such as HV and VH yields significantly larger biases (> 40 m) and RMSEs (> 60 m), indicating a more pronounced overestimation and variability, thus highlighting their inferior performance. The remarkable deviations between SAR-measured and ERA5-simulated λ_c at cross-polarizations are possibly related to the shorter lifetime of HV/VH scatters. It is worth noting that for all polarizations, the overestimation occurs at lower λ_c , whereas a significant underestimation is observed at higher λ_c . The transition points are approximately between 400–500 m.

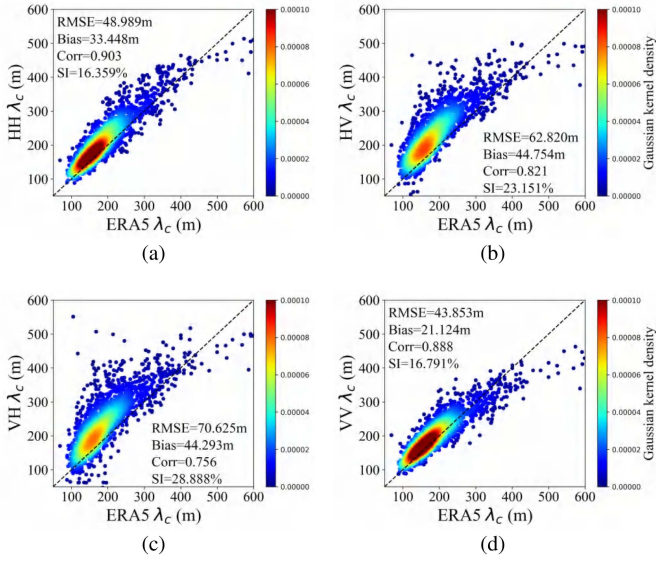


Fig. 10. Comparison of GF-3 SAR estimated λ_c and ERA5 simulated λ_c for (a) HH, (b) HV, (c) VH, and (d) VV polarizations. Dashed lines are the one-to-one curves. Color denotes data density. The panels are labeled with RMSE, Bias, Corr, and SI of GF-3 SAR estimations relative to ERA5 simulations.

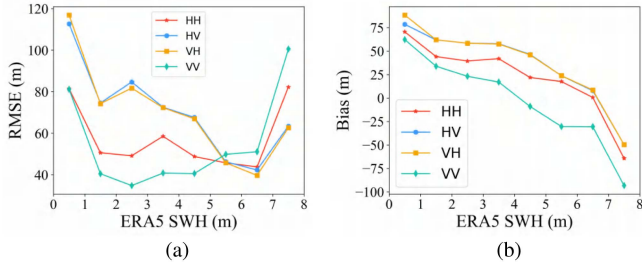


Fig. 11. (a) RMSE and (b) Bias of GF-3 SAR λ_c estimations relative to ERA5 simulations at HH, HV, VH, and VV polarizations as a function of ERA5 SWH, ranging from 0 to 8 m stepped by 1 m.

Fig. 11 shows the dependence of RMSE and Bias of GF-3 SAR λ_c estimations compared with ERA5 λ_c simulations on ERA5 SWH across the SWH range from 0 to 8 m, with a step size of 1 m, for the four polarizations of HH, HV, VH, and VV. As shown, all four polarizations display larger RMSEs and absolute biases when SWH is either too low or too high. This could be partially due to the inadequate fit of the Gaussian function to the SAR auto-correlation [44]. The Bias values exhibit a decreasing trend as ERA5 SWH increases. For lower sea states (smaller λ_c), the Bias values are positive, suggesting an overestimation of λ_c . Conversely, for higher sea states (larger λ_c), the Bias values are negative, indicating an underestimation of λ_c . The VV polarization achieves the lowest RMSEs and the smallest absolute biases at low to moderate sea states. The HH polarization follows, while the HV and VH polarizations have the highest RMSEs and the largest absolute biases. However, for high sea states, the opposite is true. The cross-polarizations yield lower RMSEs and smaller absolute biases compared with the copolarizations. These findings suggest that the copolarizations are beneficial for estimating λ_c at low to moderate sea states,

whereas the cross-polarizations are more suitable for estimating λ_c at high sea states.

B. Polarization Enhancement

Previous studies have shown that the sea surface backscatter is affected by two processes at moderate incidence angles: Bragg resonant scattering and nonBragg scattering related to breaking waves [52]. The VV polarization backscatter is primarily contributed by the Bragg resonant scattering. While it also dominates the HH polarization backscatter, the nonBragg scattering has a greater impact on HH polarization compared with VV polarization. In terms of cross-polarizations (HV and VH), the nonBragg scattering plays a more dominant role. Moreover, the nonBragg scattering is substantially enhanced with higher sea states [52]. As a result, the VV and HH backscatter become saturated at high sea states due to the dominate contribution of Bragg scattering, whereas the HV and VH backscatter remain sensitive to sea states due to the strong contribution from non-Bragg scattering related to breaking waves [53]. This implies that the wave streaks can be enhanced, and the orbital velocity-induced azimuthal displacements can be clearly visible in a cross-polarized imagette at high sea states. However, the SNR in cross-polarized imagettes is low in low to moderate sea states due to weak echo signal intensity. Meanwhile, the cross-polarization signal also significantly correlates with the internal waves and sea surface temperature front [54], [55]. These could explain why copolarization λ_c is better estimated in low to moderate sea states, whereas cross-polarization λ_c is better estimated in high sea states.

Based on the analysis above, it is plausible that the combined utilization of multiple polarization information, particularly copolarization and cross-polarization information, may reveal stronger signals of λ_c compared with using single polarization. This study refers to the method in [22] and proposes four dual-polarization and four quad-polarization combination strategies to explore the polarization enhancement effect. The four dual-polarization combination strategies are defined as follows:

$$\text{DuSP}_1 = \text{Sp}(\sigma_0^{\text{HH}}) + \frac{\overline{\sigma_0^{\text{HH}}}}{\overline{\sigma_0^{\text{HV}}}} \text{Sp}(\sigma_0^{\text{HV}}) \quad (9)$$

$$\text{DuSP}_2 = \text{Sp}(\sigma_0^{\text{HH}}) + \frac{\overline{\sigma_0^{\text{HH}}}}{\overline{\sigma_0^{\text{VV}}}} \text{Sp}(\sigma_0^{\text{VV}}) \quad (10)$$

$$\text{DuSP}_3 = \text{Sp}(\sigma_0^{\text{VV}}) + \frac{\overline{\sigma_0^{\text{VV}}}}{\overline{\sigma_0^{\text{VH}}}} \text{Sp}(\sigma_0^{\text{VH}}) \quad (11)$$

$$\text{DuSP}_4 = \text{Sp}(\sigma_0^{\text{HV}}) + \frac{\overline{\sigma_0^{\text{HV}}}}{\overline{\sigma_0^{\text{VH}}}} \text{Sp}(\sigma_0^{\text{VH}}) \quad (12)$$

where DuSP_1 , DuSP_2 , DuSP_3 , and DuSP_4 denote the enhanced dual-polarization spectra from the four dual-polarization combination strategies of HH and HV, HH and VV, VV and VH, HV and VH; $\text{Sp}(\sigma_0^{\text{HH}})$, $\text{Sp}(\sigma_0^{\text{HV}})$, $\text{Sp}(\sigma_0^{\text{VH}})$, and $\text{Sp}(\sigma_0^{\text{VV}})$ represent the cross spectra from HH, HV, VH, and VV SAR imagettes, respectively; σ_0^{HH} , σ_0^{HV} , σ_0^{VH} , and σ_0^{VV} represent the HH, HV, VH, and VV NRCS, respectively; the overbar denotes the mean

calculation. The ratio of the mean NRCS of one polarization to another in each formula is employed for equalizing the spectral magnitudes of the two polarizations. Similarly, we define four quad-polarization combination strategies as follows:

$$\text{QuSP}_1 = \text{Sp}(\sigma_0^{\text{HH}}) + \frac{\overline{\sigma_0^{\text{HH}}}}{\sigma_0^{\text{HV}} + \sigma_0^{\text{VH}} + \sigma_0^{\text{VV}}} (\text{Sp}(\sigma_0^{\text{HV}}) + \text{Sp}(\sigma_0^{\text{VH}}) + \text{Sp}(\sigma_0^{\text{VV}})) \quad (13)$$

$$\text{QuSP}_2 = \text{Sp}(\sigma_0^{\text{HV}}) + \frac{\overline{\sigma_0^{\text{HV}}}}{\sigma_0^{\text{HH}} + \sigma_0^{\text{VH}} + \sigma_0^{\text{VV}}} (\text{Sp}(\sigma_0^{\text{HH}}) + \text{Sp}(\sigma_0^{\text{VH}}) + \text{Sp}(\sigma_0^{\text{VV}})) \quad (14)$$

$$\text{QuSP}_3 = \text{Sp}(\sigma_0^{\text{VH}}) + \frac{\overline{\sigma_0^{\text{VH}}}}{\sigma_0^{\text{HH}} + \sigma_0^{\text{HV}} + \sigma_0^{\text{VV}}} (\text{Sp}(\sigma_0^{\text{HH}}) + \text{Sp}(\sigma_0^{\text{HV}}) + \text{Sp}(\sigma_0^{\text{VV}})) \quad (15)$$

$$\text{QuSP}_4 = \text{Sp}(\sigma_0^{\text{VV}}) + \frac{\overline{\sigma_0^{\text{VV}}}}{\sigma_0^{\text{HH}} + \sigma_0^{\text{HV}} + \sigma_0^{\text{VH}}} (\text{Sp}(\sigma_0^{\text{HH}}) + \text{Sp}(\sigma_0^{\text{HV}}) + \text{Sp}(\sigma_0^{\text{VH}})) \quad (16)$$

where QuSP₁, QuSP₂, QuSP₃, and QuSP₄ are the enhanced quad-polarization spectra from the four quad-polarization combination strategies, which involve combining HH with others, HV with others, VH with others, and VV with others. Then, the same procedure is applied to estimate λ_c from these combined spectra.

Fig. 12 illustrates comparisons between polarization-enhanced λ_c estimations from GF-3 SAR and λ_c simulations from ERA5 for different polarization combinations. It can be seen that most of the proposed polarization combinations yield lower RMSEs, reduced biases, higher Corrs, and smaller SIs when compared with their respective single-polarization counterpart, indicating clear polarization enhancement in the performance of λ_c estimation. Among the four dual-polarization combinations, the VV + VH combination demonstrates the greatest improvement with the lowest RMSE of 34.040 m, the least bias of 18.875 m, and the smallest SI of 15.813%. The HH + VV combination exhibits slightly higher RMSE, Bias, and SI compared with VV + VH. The HH + HV combination shows even higher RMSE, Bias, and SI. These three dual-polarization combinations generally exhibit better performance than all the four single polarizations, including the best-performing VV polarization. On the other hand, the HV + VH combination exhibits the highest RMSE of 60.825 m, the maximal Bias of 43.340 m, the smallest Corrs of 0.831 m, and the largest SI of 22.412%. The combination of VV polarization and cross-polarization yields the most significant enhancement due to the fact that the VV polarization produces the best outcome among the four single polarizations, and the combination of copolarization and cross-polarization can effectively work over the entire sea states, with copolarization being effective in low to moderate sea states and cross-polarization being effective in high sea states.

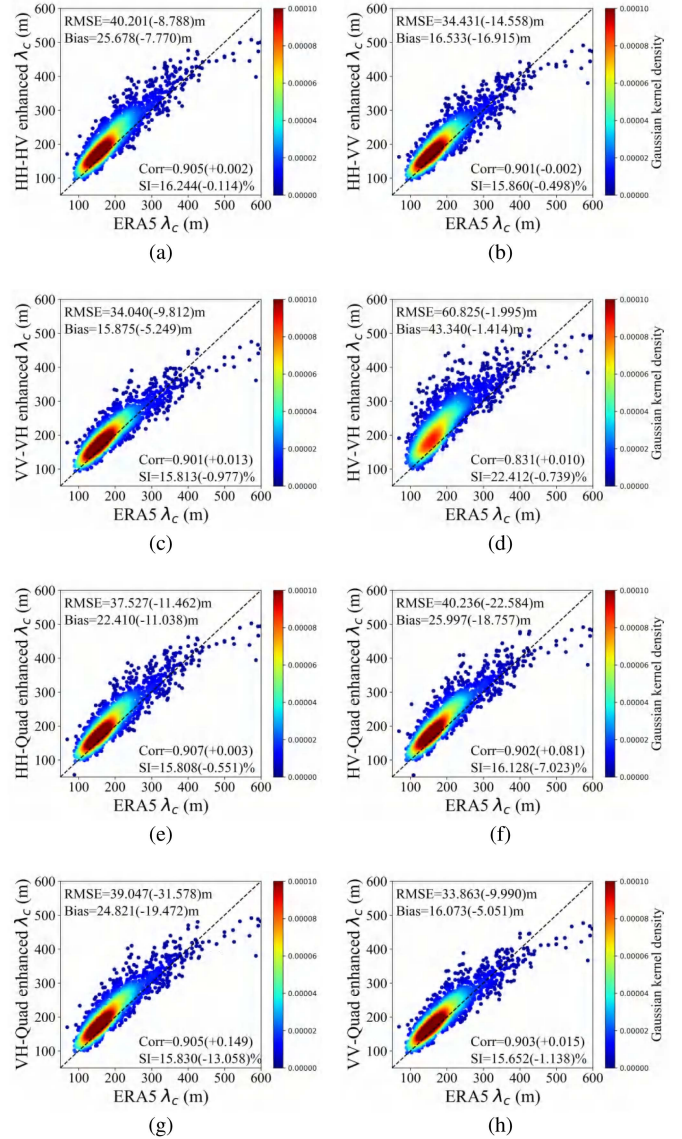


Fig. 12. Comparison of polarization enhanced λ_c estimations and ERA5 λ_c simulations for different combinations of (a) HH and HV, (b) HH and VV, (c) VV and VH, (d) HV and VH, (e) HH and others, (f) HV and others, (g) VH and others, and (h) VV and others. The numbers in brackets represent the numerical changes compared with the first single polarization in the corresponding polarization combination formula. The labels are the same as those in Fig. 10.

Among the four quad-polarization combinations, the combinations of copolarization (HH or VV) with other polarizations exhibit superior performance when compared with the combinations of cross-polarization (HV or VH) with other polarizations in terms of smaller RMSEs, biases, and SIs. The combination of VV polarization with other polarizations yields the lowest RMSE of 33.863 m, the least bias of 16.073 m, and the smallest SI of 15.652%. This suggests that prioritizing VV polarization and incorporating other polarization information provides the most comprehensive azimuth cutoff information and achieves the most significant enhancement in estimating λ_c . When compared with the combination of VV + VH, the combination of VV + (HH + VH + HV) results in a 0.18 m lower RMSE and a 0.16% smaller SI, but a 0.20 m larger bias.

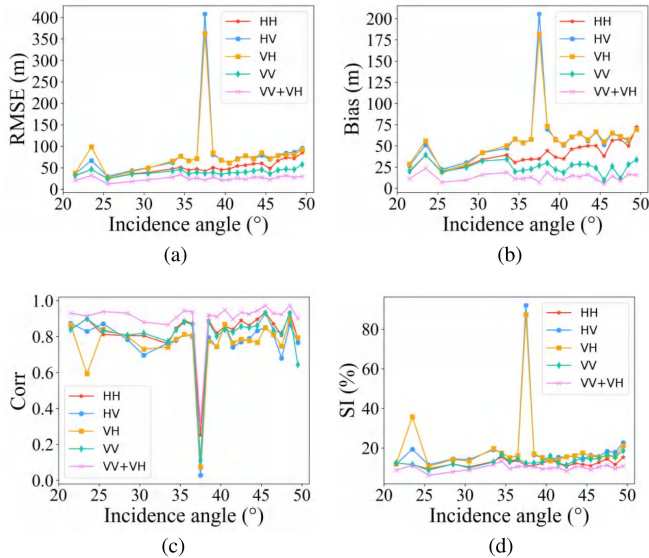


Fig. 13. (a) RMSE, (b) Bias, (c) Corr, and (d) SI of GF-3 SAR estimated λ_c relative to ERA5 simulated λ_c with respect to incidence angle for the four single polarizations of HH, HV, VH, and VV, as well as the optimal polarization combination of VV + VH.

This suggests that the inclusion of two additional polarizations does not significantly enhance the accuracy of λ_c estimation. The VV + VH dual-polarization combination, which shows the greatest cost performance, is ultimately selected as the optimal combination for λ_c estimation from GF-3 SAR.

Fig. 13 illustrates the RMSE, Bias, Corr, and SI of GF-3 SAR estimated λ_c compared with ERA5 simulated λ_c across various incidence angle ranges for the four single polarizations of HH, HV, VH, and VV, as well as the optimal polarization combination of VV + VH. As can be seen, the error metrics for all four single polarizations show an increasing trend with incidence angle, which can be explained by the decrease in NESZ and sea backscattering, as well as the SNR with increasing incidence angle. Meanwhile, the dual-polarization combination of VV + VH reduces the impact of incidence angle on the error metrics. Significant outliers are observed near the incidence angle of 37.5° , which is due to the abnormal intensity distribution of GF-3 SAR WM imagettes at 37.5° incidence angle in this dataset, especially in cross-polarization imagettes, ultimately resulting in abnormally large λ_c values.

Table I presents the error metrics of GF-3 SAR estimated λ_c relative to ERA5 simulated λ_c in wind wave seas and swell seas for the four single polarizations: HH, HV, VH, and VV, as well as the optimal polarization combination of VV + VH. It can be seen that the performance of λ_c estimation is much better in wind wave seas than in swell seas. This might be due to the fact that the azimuth cutoff behavior primarily reflects the nonlinear transformation of local wind waves and SAR imagettes. The optimized λ_c estimation method can effectively improve the accuracy of λ_c estimation in both sea states. All up, the optimized estimation of λ_c is achieved by combining the cross spectra of VV and VH polarization GF-3 SAR imagettes with a pixel spacing of 12 m, and implementing an adaptive median filter before Gaussian fitting.

TABLE I
ERROR METRICS OF GF-3 SAR ESTIMATED λ_c RELATIVE TO ERA5
SIMULATED λ_c IN WIND WAVE SEAS AND SWELL SEAS FOR THE FOUR SINGLE
POLARIZATIONS OF HH, HV, VH, AND VV, AS WELL AS THE OPTIMAL
POLARIZATION COMBINATION OF VV + VH

Polarization	Sea State	RMSE (m)	Bias (m)	Corr	SI (%)
HH	Wind Sea	39.453	27.089	0.822	13.173
	Swell Sea	45.689	30.874	0.734	14.635
HV	Wind Sea	58.409	29.646	0.726	15.867
	Swell Sea	71.426	52.183	0.604	19.803
VH	Wind Sea	57.960	28.964	0.730	15.863
	Swell Sea	72.941	52.160	0.585	20.704
VV	Wind Sea	50.144	27.677	0.854	16.092
	Swell Sea	54.279	28.831	0.740	16.322
VV+VH	Wind Sea	35.289	14.757	0.909	14.304
	Swell Sea	41.713	15.874	0.853	15.010

IV. IMPACT OF POLARIZATION ENHANCEMENT ON CORRELATION

In this section, the effects of polarization and polarization enhancement on the correlation between the λ_c and the wave and wind parameters are analyzed based on the GF-3 SAR WM imagettes matched with the SWH and WS data from ERA5 reanalysis. And analyzed the correlation between incidence angle, wind direction, wave direction, and λ_c .

A. SWH and WS

Fig. 14 illustrates the dependence of λ_c on SWH (left panels) and on WS (right panels) for the four single polarizations of HH, HV, VH, and VV, as well as the optimal polarization combination of VV + VH. Usually, the correlation between the λ_c and square root of SWH is estimated [56]. But after testing, the correlation between the λ_c and SWH is similar to the correlation on the λ_c and square root of SWH. In order to describe it concisely, the Corr (R) between the λ_c and SWH is calculated. It can be seen that the λ_c generally exhibits a positive linear dependence with SWH (WS) at all polarization states. However, the SWH (WS) dependent properties vary across different polarization states. The copolarizations like HH and VV show higher correlations compared with the cross-polarizations like HV and VH, which suggests that the dependence of copolarization λ_c on SWH (WS) is stronger than that of cross-polarization λ_c . This is consistent with the findings in [41]. This difference could be attributed to the lower SNR of cross-polarized SAR imagettes in low to moderate sea states. Furthermore, the Corrs of cross-polarization λ_c with WS are around 0.70, whereas the Corrs with SWH are around 0.63, indicating a stronger association between cross-polarization λ_c and WS compared with SWH. However, this is not true for copolarizations. It suggests that the cross-polarization observations are more sensitive to winds than to waves. What is more, the polarization-enhanced λ_c estimations exhibit larger Corrs (about 0.84) and more clustered scatter distributions with SWH and WS. This clearly demonstrates

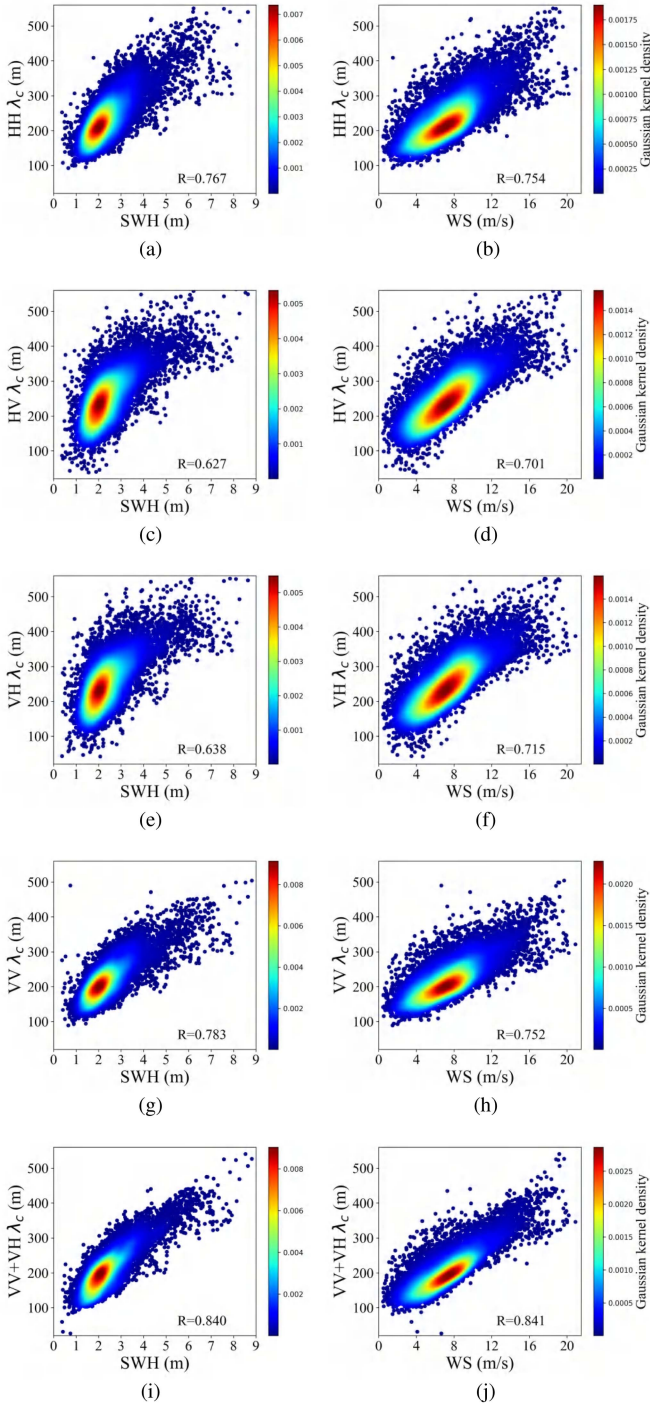


Fig. 14. Scatter plots of the λ_c estimations from GF-3 SAR WM imagettes against SWH (left panels) and WS (right panels) under the four single polarizations of HH, HV, VH, and VV, as well as the optimal polarization combination of VV + VH. The R is the Corr between λ_c and SWH (WS). (a) HH SWH, (b) HH WS, (c) HV SWH, (d) HV WS, (e) VH SWH, (f) VH WS, (g) VV SWH, (h) VV WS, (i) VV+VH SWH, and (j) VV+VH WS.

that the polarization-enhanced estimation of λ_c can effectively improve its dependence on SWH and WS.

Table II displays the Corrs of the estimated λ_c with SWH and WS in wind wave seas and swell seas for the four single polarizations (HH, HV, VH, and VV) and the optimal polarization combination of VV + VH. It can be seen that the correlation

TABLE II
CORR OF λ_c WITH SWH AND WS IN WIND WAVE DOMINATED SEAS AND SWELL DOMINATED SEAS FOR HH, HV, VH, AND VV POLARIZATIONS AND THE OPTIMAL POLARIZATION COMBINATION OF VV + VH

Polarization	Sea State	SWH R	WS R
HH	Wind Sea	0.836	0.770
	Swell Sea	0.755	0.736
HV	Wind Sea	0.814	0.773
	Swell Sea	0.611	0.686
VH	Wind Sea	0.810	0.770
	Swell Sea	0.623	0.701
VV	Wind Sea	0.866	0.807
	Swell Sea	0.772	0.735
VV+VH	Wind Sea	0.927	0.890
	Swell Sea	0.831	0.827

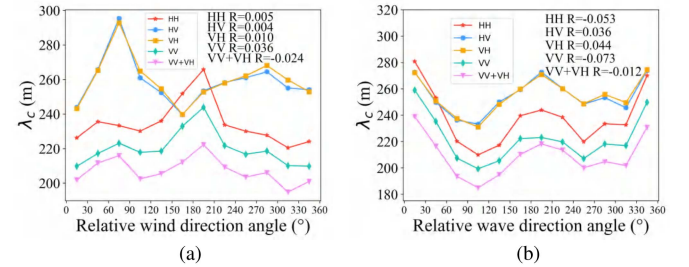


Fig. 15. GF-3 SAR estimated λ_c versus (a) relative wind direction and (b) relative wave direction for HH (red lines), HV (blue lines), VH (yellow lines), VV (green lines), and VV + VH (pink lines) polarizations. The R is the Corr between λ_c and relative wind direction (relative wave direction).

of λ_c with SWH (WS) is significantly stronger in wind wave seas compared with in swell seas under all polarization states. This may suggest that the azimuthal cutoff is more caused by the movement of the wind waves. In addition, the correlation of λ_c with SWH is generally higher than that with WS, except for cross-polarization λ_c in swell-dominated sea states where the opposite is true. This might be due to the direct SAR imaging of sea surface waves and the indirect impact of wind on the imagery through its influence on wave dynamics, however, the cross-polarization data are more sensitive to winds. The polarization-enhanced λ_c shows a clearly higher correlation with both SWH and WS in both sea states, indicating that the polarization enhancement weakens the influence of sea states.

B. Wind Direction and Wave Direction

Fig. 15 illustrates the dependence of the estimated λ_c on relative wind direction and relative wave direction for the four single polarizations of HH, HV, VH, and VV, as well as the optimal polarization combination of VV + VH. The relative wind direction angle is defined as $\phi_u = \varphi_{\text{wind}} - \varphi_{\text{radar}}$, where φ_{wind} is the direction the wind is coming from, φ_{radar} is the satellite azimuth look direction, both with respect to the North. $\phi_u = 0$ corresponds to an upwind observation for which the wind is blowing toward the radar. The relative wave direction angle is defined as $\phi_w = \varphi_{\text{wave}} - \varphi_{\text{radar}}$, where φ_{wave} is the direction

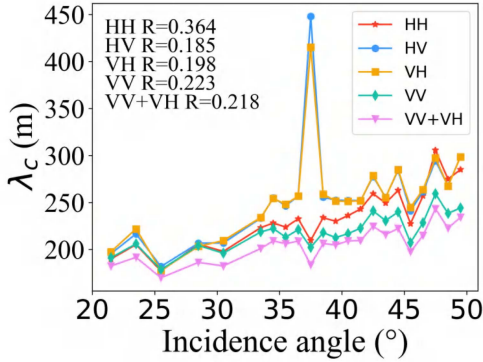


Fig. 16. GF-3 SAR estimated λ_c versus incidence angle for HH (red lines), HV (blue lines), VH (yellow lines), VV (green lines), and VV + VH (pink lines) polarizations. The R is the Corr between λ_c and incidence angle.

the wave is coming from. $\phi_w = 0$ corresponds to an upwave observation for which the wave is moving toward the radar. The estimated λ_c is averaged across a range of 30° relative wind/wave directions, encompassing all WSs and incidence angles. As shown, λ_c fluctuates with the wind direction and wave direction, mostly within a range of 40 m. The correlation between λ_c and wind direction does not exhibit a clear pattern, and their Corrs are extremely low, with a maximum value of 0.036, suggesting a weak dependence of λ_c on wind direction. The relationship between λ_c and wave direction relationship biharmonic behavior, with larger values around upwave/downwave directions, and smaller values around crosswave directions. The Corrs between λ_c and wave direction are still very small, not exceeding 0.1, although larger compared with those of wind direction, suggesting a weak dependence of λ_c on wave direction. Moreover, the polarization enhancement reduces the λ_c value in all wind and wave directions, but it has almost no effect on the correlation between λ_c and wind direction or wave direction.

C. Incidence Angle

Fig. 16 presents the dependence of the estimated λ_c on incidence angle for HH, HV, VH, VV, and VV + VH polarizations. The λ_c values are averaged within 1° incidence angle bins, covering all WSs and wind/wave directions. As shown, λ_c generally increases with the incidence angle for all polarizations. The λ_c positively correlates with incidence angle for all polarizations, with the HH channel demonstrating the highest Corr, followed by VV, whereas the cross-polarization channels exhibit comparatively lower Corrs. The VV+VH compromises those of VV and VH. These findings suggest that the incidence angle significantly affects the λ_c estimation. Fig. 17 depicts the correlation of λ_c with SWH and WS under different incidence angles. As seen, the correlation between λ_c and SWH (WS) fluctuates with the incidence angle. The copolarization λ_c generally exhibits a higher correlation with SWH than the cross-polarization λ_c , but a lower correlation with WS at most incidence angles. The polarization-enhanced λ_c demonstrates an even higher correlation. Similarly, there are noticeable outliers present around the incidence angle of 37.5° which cannot be

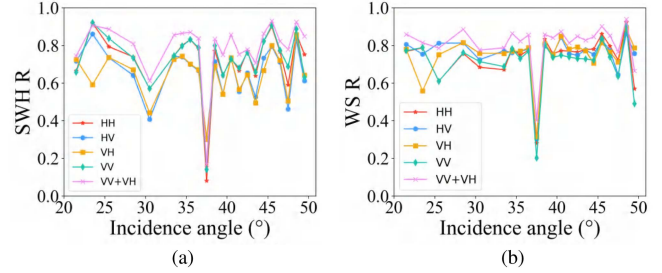


Fig. 17. Corr of λ_c with (a) SWH and (b) WS as functions of incidence angle for HH (red lines), HV (blue lines), VH (yellow lines), VV (green lines), and VV + VH (pink lines) polarizations.

improved. Therefore, the 58 match-up data points around 37.5° incidence angle is removed in the following study.

V. IMPACT OF POLARIZATION ENHANCEMENT ON SWH AND WS RETRIEVAL ALGORITHMS

This section aims to verify whether the polarization-enhanced estimation of λ_c can improve the capability of SWH and WS retrieval. Three algorithms, including single linear regression (SLR) [7], [19], [56], multiple linear regression (MLR) [57], and Gaussian process regression (GPR) [25], are used to develop the retrieval models for extracting SWH and WS from λ_c estimated from GF-3 SAR WM imageries for the four single polarizations of HH, HV, VH, and VV, as well as the optimal polarization combination of VV + VH. The retrieval models are constructed based on the 11105 SAR-ERA5 collocated data points. This collocated dataset is randomly partitioned into two distinct subsets: one for model training (70%) and the other for testing (30%).

Based on SLR, the SWH or the WS is linearly related to the λ_c merely, as formulated below:

$$X = a\lambda_c + b \quad (17)$$

where X is the SWH or the WS, and a and b are model coefficients, which are determined from the training dataset using the least square method. It would be better to additionally take NRCS and incidence angle θ into account when constructing empirical models for SWH and WS retrieval from GF-3 SAR. The experiment results show that the wind direction and wave direction have almost no effect on the inversion results, so they are not introduced into the model. Based on MLR, the relationship between SWH (WS) and SAR parameters including λ_c , NRCS (VV+VH polarization using a combination of VV polarization NRCS and VH polarization NRCS) and θ can be formulated as follows:

$$X = a_0 + \sum_{i=1}^M a_i k_i + \sum_{i=1}^M \sum_{j=1}^i a_{i,j} k_i k_j \quad (18)$$

where X is the SWH or the WS, k_i is the SAR parameter, $a_{i,j}$ is the tuned coefficient, and $M = 3$ is the number of SAR parameters. GPR is a machine learning model known for its strong adaptability and ability to effectively handle high-dimensional nonlinear data. It utilizes a flexible semianalytical Bayesian approach that involves nonlinear mapping to establish

the relationship between input and output data [58] as follows:

$$y = f(X) + \varepsilon \quad (19)$$

where y is the model output, X is the model input, $f(X)$ is a Gaussian process that can be specified by its mean (which is taken to be zero) and covariance matrix K , and ε is the independent identically distributed Gaussian noise with zero mean and constant variance. For this model, the SAR parameters including λ_c , NRCS (VV+VH polarization using a combination of VV polarization NRCS and VH polarization NRCS) and θ are used as the input, and the ERA5 SWH and WS is used as the training output. The elements of K can be computed by using a kernel function. The anisotropic exponential kernel is used here.

Figs. 18–20 display scatter density plots of GF-3 SAR SWH and WS retrievals against ERA5 SWH and WS for the four single-polarization modes (HH, HV, VH, and VV) and the optimal polarization combination (VV+VH) using the SLR, MLR, and GPR models. It can be seen that across all models, the copolarization models (HH and VV) exhibit better performance than the cross-polarization models (HV and VH). The VV polarization provides the best SWH estimation, whereas the HH polarization delivers the best WS estimation out of the four single-polarizations. These are consistent to the correlation analysis results. The inferior performance of cross-polarization models in retrieving SWH and WS can be attributed to the weaker dependence of cross-polarization λ_c , which is associated with the lower SNR observed in cross-polarized SAR imagettes under low to moderate sea states. Furthermore, it is undeniable that the polarization combination of VV+VH achieves improved performance for both SWH and WS estimation, with the lowest RMSEs, the largest Corrs, and the smallest SIs. This reveals that the utilization of polarization-enhanced λ_c can further augment the performance of SWH and WS estimation derived from GF-3 SAR WM data. This is consistent with the results in [22].

Overestimation (underestimation) is observed under low (high) sea conditions. This might be related to the inadequate distribution of data, with mere a 1% chance in low sea states and a 10% chance in high sea states compared with moderate sea states. The significant variations in data density can lead to solutions that are biased toward regions with higher density and result in poorly functioning empirical models [16]. According to the conclusion obtained from Fig. 11, cross-polarization is more accurate in estimating λ_c under high sea states compared with copolarization. Therefore, we expect cross-polarization models to exhibit better retrieval accuracy under high sea states. However, through the scatter distribution under high sea states in Figs. 18 and 19, it can be observed that cross-polarization models do not show an advantage in retrieval accuracy, as they exhibit larger underestimation despite smaller dispersion. This might be due to the significant positive Bias of the λ_c in cross-polarization estimation under low to moderate sea states, resulting in a decrease in the slope of the linear models, and a more pronounced underestimation under high sea states. Establishing models using polarization-enhanced λ_c can improve this phenomenon. The scatter distributions in Figs. 18–20 reveals a

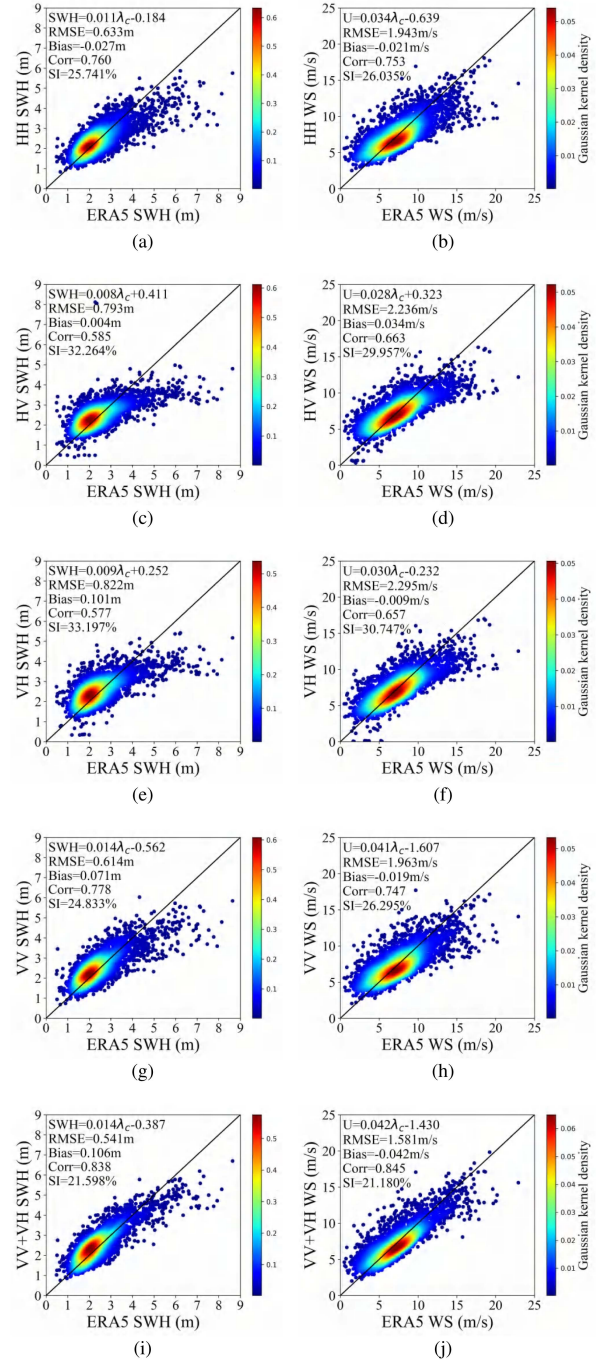


Fig. 18. Scatter plots of GF-3 SAR SWH and WS retrievals from SLR models against ERA5 SWH and WS for the four single-polarization modes of HH, HV, VH, and VV, and the optimal polarization combination of VV+VH. (a) HH SWH, (b) HH WS, (c) HV SWH, (d) HV WS, (e) VH SWH, (f) VH WS, (g) VV SWH, (h) VV WS, (i) VV+VH SWH, and (j) VV+VH WS.

clear polarization enhancement across low to high sea states, as evidenced by the closely clustered data points aligning with the 1:1 lines.

In all polarization cases, GPR models consistently demonstrate superior performance, followed by MLR models, whereas SLR models exhibit relatively inferior performance. Although the SLR models have the weakest performance, the RMSE and

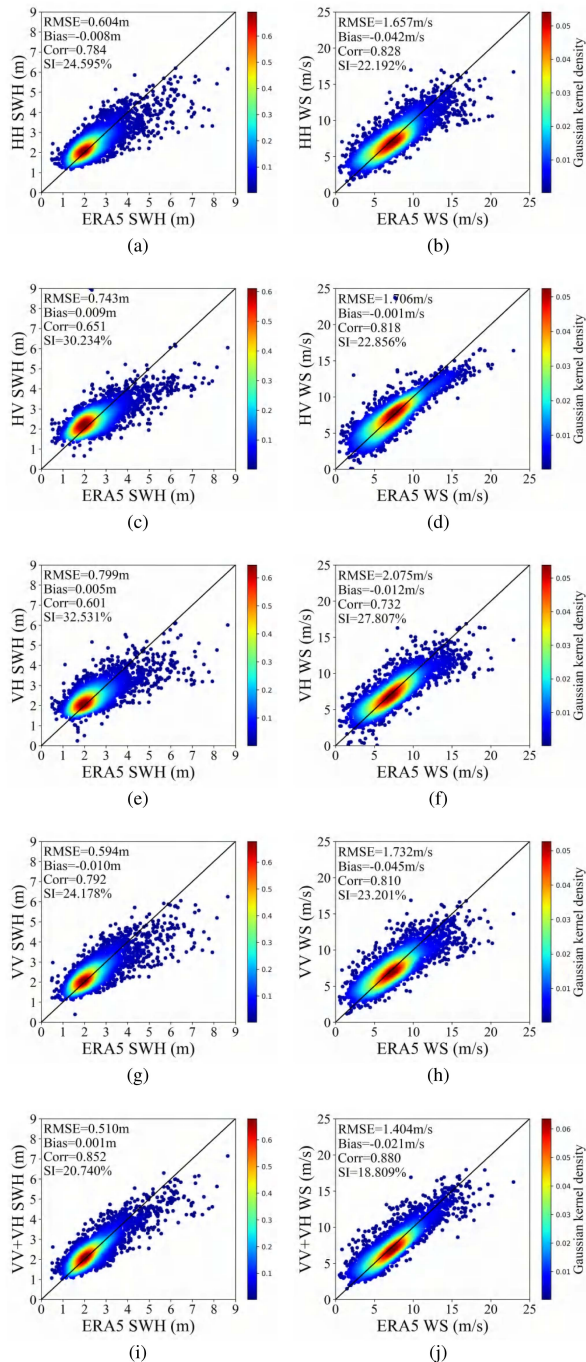


Fig. 19. Scatter plots of GF-3 SAR SWH and WS retrievals from MLR models against ERA5 SWH and WS for the four single-polarization modes of HH, HV, VH, and VV, and the optimal polarization combination of VV+VH. (a) HH SWH, (b) HH WS, (c) HV SWH, (d) HV WS, (e) VH SWH, (f) VH WS, (g) VV SWH, (h) VV WS, (i) VV+VH SWH, and (j) VV+VH WS.

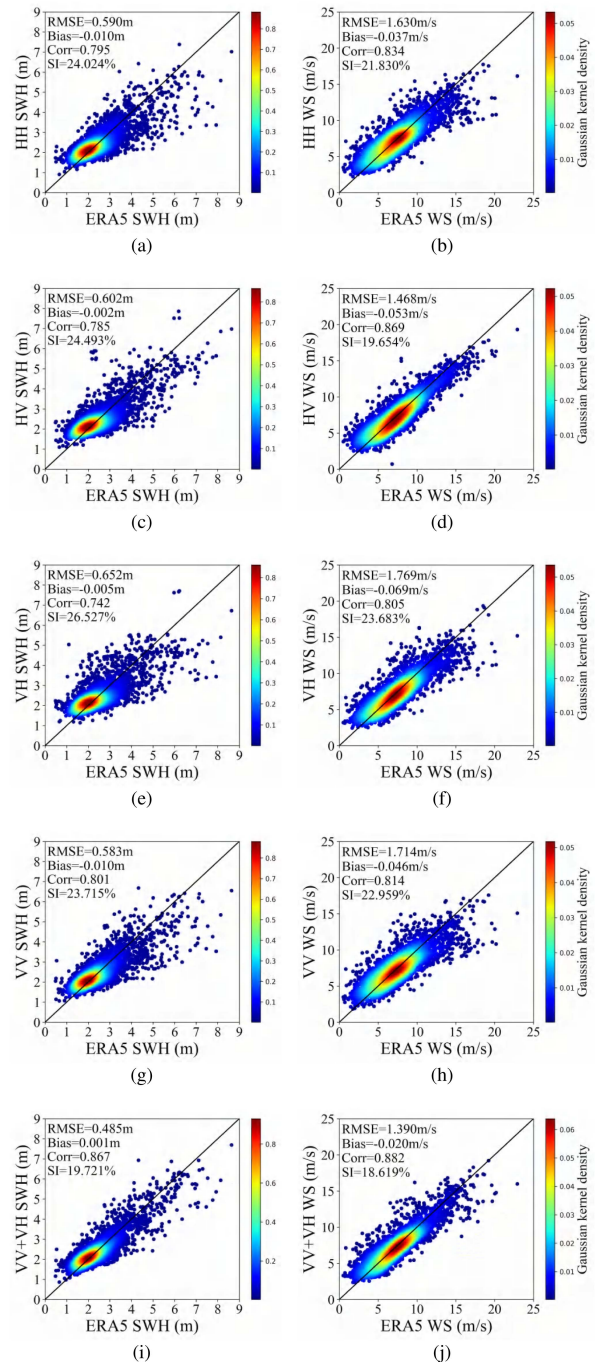


Fig. 20. Scatter plots of GF-3 SAR SWH and WS retrievals from GPR models against ERA5 SWH and WS for the four single-polarization modes of HH, HV, VH, and VV, and the optimal polarization combination of VV+VH. (a) HH SWH, (b) HH WS, (c) HV SWH, (d) HV WS, (e) VH SWH, (f) VH WS, (g) VV SWH, (h) VV WS, (i) VV+VH SWH, and (j) VV+VH WS.

Corr of SWH and WS retrieval using the optimal polarization combination of VV+VH of the SLR model still outperform all the single-polarization retrievals of MLR and GPR models, except for the GPR model's HV polarization WS retrieval. This demonstrates the significant improvement in retrieval performance achieved by the optimal polarization combination of VV+VH. The enhanced performance of MLR over SLR can be attributed to the additional consideration of NRCS and θ , as

well as the incorporation among the features. These factors effectively supplement extra information for enhancing the retrieval accuracy of SWH and WS. The exceptional performance of GPR is due to the added nonlinearity of the GPR, which models SWH and WS more accurately than the polynomial regression.

For SWH retrieval, the SLR model with polarization-enhanced λ_c input achieves a RMSE of 0.541 m, a Bias of 0.106 m, a Corr of 0.838, and a SI of 21.598% on SAR-ERA5 test

dataset. The MLR model with polarization-enhanced λ_c input achieves a RMSE of 0.510 m, a bias of 0.001 m, a Corr of 0.852, and a SI of 20.740% on SAR-ERA5 test dataset. The GPR model with polarization-enhanced λ_c input achieves a RMSE of 0.485 m, a bias of 0.001 m, a Corr of 0.867, and a SI of 19.721% on SAR-ERA5 test dataset. The SLR model with polarization-enhanced λ_c performs better than the retrieval algorithms using the linear model for Sentinel-1 SAR imagerettes [20]. GF-3 SAR imagerettes have no data quality advantage compared with Sentinel-1 SAR imagerettes. The advantage of our SLR model mainly comes from the combination of VV and VH polarization, which leads to more accurate λ_c . The performance of these models surpasses that of the previous λ_c -based algorithms proposed in [19], [20], [21], [22], [59], etc., with their RMSEs mostly falling within the range of 0.55–0.90 m. Moreover, our polarization-enhanced GPR model, which utilizes only three SAR features as input, achieves comparable performance to the CWAVE models developed in [14], [15], [16], and [17] that use 22 or more features as input. Although our polarization-enhanced GPR model falls short of the performance achieved by previous state-of-the-art algorithms (with RMSEs of around 0.30 m) developed in [25], [26], [27], [28], [29], etc., which leverage more SAR features, more polarization information, or more complex algorithm structures, we believe that it exhibits exceptional cost-effectiveness.

For WS retrieval, the SLR model with polarization-enhanced λ_c input achieves a RMSE of 1.581 m/s, a bias of -0.042 m/s, a Corr of 0.845, and a SI of 21.180% on SAR-ERA5 test dataset. The MLR model with polarization-enhanced λ_c input achieves a RMSE of 1.404 m/s, a bias of -0.021 m/s, a Corr of 0.880, and a SI of 218.809%. The GPR model with polarization-enhanced λ_c input achieves a RMSE of 1.390 m/s, a bias of -0.020 m/s, a Corr of 0.882, and a SI of 18.619%. These models outperform previous λ_c -based algorithms proposed in [23], [43], [59], etc., with RMSEs approximately around 2 m/s. Moreover, our polarization-enhanced GPR model achieves comparable or even superior SAR WS estimation compared with the NRCS-based algorithms developed in [32], [33], [34], [35], [36], [37], [38], [39], [40], and [41], with RMSEs approximately within 1.3–3.0 m/s, while eliminating the need for wind direction input.

VI. DISCUSSIONS

In order to find out the impact of unbalanced distribution of sea states in the dataset on the performance of the retrieval algorithm, we create a dataset containing 2340 imagerettes with a more balanced distribution of sea states, as shown in Fig. 21. And the new dataset is used to establish SLR SWH retrieval algorithm as an example to explore the impact of sea states distribution on the performance of the retrieval algorithm. Table III presents the performance of the VV+VH polarization SLR SWH retrieval algorithm for two datasets under different SWH ranges. It can be clearly seen from the table that the RMSE of the algorithm using the new dataset is 0.640 m, which is worse than the 0.541 m using the original dataset, but the Corr and SI of retrieved SWH are better. For cases with small sample number of $\text{SWH} \leq 1.5$ m and $\text{SWH} > 4.5$ m, the algorithm using the

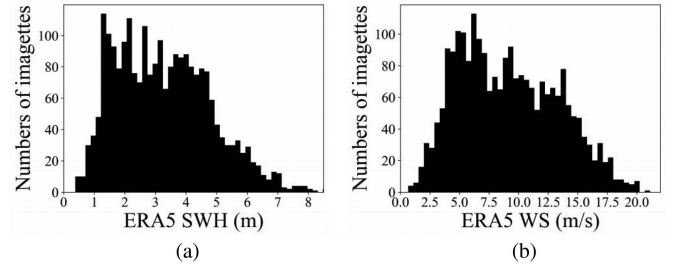


Fig. 21. Distribution of GF-3 WM imagerettes in new and more balanced dataset matched with ERA5 data. (a) Histogram of ERA5 SWH. (b) Histogram of ERA5 WS.

TABLE III
ERROR METRICS OF SLR ALGORITHM RETRIEVED SWH RELATIVE TO ERA5 SWH IN OPTIMAL POLARIZATION COMBINATION OF VV + VH

SWH(m)	Sample number	RMSE(m)	Bias(m)	Corr	SI(%)
Original dataset SLR SWH Retrieval VV+VH Polarization					
$\text{SWH} \leq 1.5$	263	0.572	0.377	0.152	33.419
$1.5 < \text{SWH} \leq 3$	2396	0.473	0.182	0.565	20.257
$3 < \text{SWH} \leq 4.5$	536	0.519	-0.071	0.528	14.618
$4.5 < \text{SWH}$	153	1.181	-0.937	0.583	13.097
Total	3348	0.541	0.106	0.838	21.598
New dataset SLR SWH Retrieval VV+VH Polarization					
$\text{SWH} \leq 1.5$	88	0.519	0.241	0.298	38.704
$1.5 < \text{SWH} \leq 3$	225	0.522	0.049	0.556	23.178
$3 < \text{SWH} \leq 4.5$	225	0.524	0.102	0.579	13.856
$4.5 < \text{SWH}$	164	0.927	-0.551	0.645	13.362
Total	702	0.640	-0.049	0.916	18.998

new dataset shows a significant advantage in retrieval accuracy, due to the more balanced distribution of sea states. When $1.5 \text{ m} < \text{SWH} \leq 3 \text{ m}$, the original dataset has a significant advantage in terms of data volume compared with the new dataset, resulting in the algorithm using the original dataset exhibiting better retrieval accuracy. Based on the test results, we can find that the distribution of sea states and the number of datasets greatly affect the performance of the retrieval algorithm. A dataset with a balanced distribution of sea states and a large amount of data can bring out the optimal performance of retrieval algorithm.

VII. CONCLUSION

This study develops an optimal estimation method for the λ_c with a focus on the combination of multipolarization. The impact of polarization enhancement on the correlation between the λ_c and SWH and WS are analyzed. Three λ_c -based SWH and WS retrieval algorithms are established, and the performance of the algorithms is thoroughly discussed. Compared with relevant studies [22], [23], [43], [44], this study provides a more comprehensive analysis of the factors affecting λ_c estimation and explores the performance of polarization enhancement through correlation analysis and SWH (WS) retrieval.

Before studying the polarization combination method, an analysis of the impact of pixel spacing and median filter on

the estimation of the λ_c is conducted. It is found that the accuracy of the λ_c estimation improves and then deteriorates with increasing pixel spacing, reaching optimal performance near 12 m. Furthermore, the adaptive median filter also slightly optimizes the accuracy of the λ_c estimation at 12 m pixel spacing. Through the analysis of the accuracy of the λ_c estimation for different polarizations, it is found that copolarization λ_c has an estimation advantage in low to moderate sea states, whereas cross-polarization λ_c has an estimation advantage in high sea states. Based on this finding, four dual-polarization combinations and four quad-polarization combinations of polarization-enhanced λ_c estimation methods are proposed and tested. The results indicate that multipolarization combinations, especially copolarization and cross-polarization combinations, can achieve more accurate λ_c estimation, with the VV+VH polarization combination showing the best cost performance. Finally, it is established to use 12 m pixel spacing, apply adaptive median filtering to Gaussian-fitted data, and utilize the VV+VH polarization combination as the core of the optimized λ_c estimation method.

After obtaining the optimized estimation of the λ_c , an analysis is conducted on the correlation between different polarized λ_c , including VV+VH polarization, and SWH (WS), as well as the correlation between the λ_c and wind direction, wave direction, and incidence angle. It is found that there is a clear positive correlation between the λ_c and SWH (WS), with VV+VH polarization showing the strongest correlation, followed by copolarization, and cross-polarization exhibiting the weakest correlation. At the same time, the λ_c also shows a certain positive correlation with the incidence angle, whereas the correlation with wind direction and wave direction is very weak. Therefore, the incidence angle is considered when establishing the retrieval model. Three retrieval models based on the λ_c for SWH and WS are established, including SLR, MLR, and GPR. The MLR and GPR models, in addition to the λ_c , also incorporate NRCS and incidence angle. Among the three models, VV+VH polarization demonstrates the best retrieval accuracy, followed by copolarization, and cross-polarization exhibits the poorest retrieval accuracy. For the three models, the SLR model exhibits the poorest retrieval accuracy. The MLR model shows an improved retrieval accuracy compared with the SLR model due to the inclusion of NRCS and incidence angle. The GPR model achieves the best retrieval accuracy by incorporating nonlinear Gaussian regression process.

The experimental results demonstrate the superior performance of polarization-enhanced λ_c -based SWH and WS retrieval algorithms. The GPR model, in particular, achieves lower RMSE, bias, and higher Corrs compared with previous λ_c -based algorithms. Although our polarization-enhanced λ_c GPR model falls short of the performance achieved by state-of-the-art algorithms, which leverage more SAR features, more polarization information, or more complex algorithm structures, we believe that it exhibits exceptional cost-effectiveness. These models also outperform NRCS-based algorithms for WS retrieval, while eliminating the need for wind direction input. However, this study still has several limitations. First, the distribution of sea states in GF-3 dataset is not balanced, with too few data available

under low and high sea states. Second, the validation data is based on ERA5 data rather than observational measurements. Third, the number of parameters involved in the retrieval is limited, leaving room for further improvement in the retrieval model.

In the future, we plan to collect more data, establish a dataset with balanced sea states distribution to address the above issues. We believe that the polarized-enhanced λ_c estimation method proposed in this article is also applicable to other C-band quad- or dual-polarization SAR data, but its specific applicability needs to be discussed in the next step. Previous studies have shown that SAR can use the NRCS-based algorithms to retrieve SWH and WS under extreme sea states such as typhoons, cyclones, hurricanes, etc. [24], [60], [61], but the NRCS-based algorithms have limitations. The λ_c -based algorithms are considered to have large potential for retrieving SWH and WS in high sea states [43]. We will test the applicability of the algorithms proposed in this article under extreme sea states.

APPENDIX

The method proposed by Xiaoqing Chu is employed to differentiate between wind waves and swell on sea state in the study [51] as follows:

$$H^* = \frac{1}{16} \left(\frac{gH_s}{U_{10}^2} \right)^2$$

$$\beta_{\text{inv}} = \frac{U_{10}}{C_p}, C_p = \frac{2\pi}{T_p k_p}, k_p = \frac{(2\pi/T_p)^2}{g} \quad (20)$$

where H_s is the SWH, U_{10} is the WS at 10 m height above the sea surface, C_p is the phase velocity of the dominant wave, T_p is the wave period of the dominant wave, and k_p is the wave number of the dominant wave. H_s , U_{10} , and T_p can be obtained by ERA5 reanalysis data, and g takes 9.8 m/s². The sea state is dominated by swells when $H^* > 3.64 \times 10^{-3}$ and $\beta_{\text{inv}} < 0.82$; otherwise, it is dominated by wind waves.

ACKNOWLEDGMENT

The authors would like to thank Chinese National Satellite Ocean Application Service (NSOAS) for providing the GF-3 SAR WM data (registration required).¹ The authors would also like to thank ECMWF for providing the ERA5 data.

REFERENCES

- [1] I. R. Young and A. Ribal, "Multiplatform evaluation of global trends in wind speed and wave height," *Science*, vol. 9527, no. 4, pp. 1–10, 2019.
- [2] F. T. Ulaby and D. G. Long, *Microwave Radar and Radiometric Remote Sensing*. Ann Arbor, MI, USA: Univ. of Michigan Press, 2014, pp. 664–669.
- [3] W. R. Alpers, D. B. Ross, and C. L. Rufenach, "On the detectability of ocean surface waves by real and synthetic aperture radar," *J. Geophys. Res.*, vol. 86, pp. 6481–6498, 1981.
- [4] K. Hasselmann et al., "Theory of synthetic aperture radar ocean imaging: A. MARSEN view," *J. Geophys. Res.*, vol. 90, pp. 4659–4686, 1985.

¹[Online]. Available at <https://osdds.nsoas.org.cn/>

- [5] W. Alpers and C. Bruening, "On the relative importance of motion related contributions to the SAR imaging mechanism of ocean surface waves," *IEEE Trans. Geosci. Remote Sens.*, vol. GE-24, no. 6, pp. 873–885, Nov. 1986.
- [6] K. Hasselmann and S. Hasselmann, "On the nonlinear mapping of an ocean wave spectrum into a synthetic aperture radar image spectrum and its inversion," *J. Geophys. Res.*, vol. 96, no. C6, pp. 10 713–10 729, 1991.
- [7] V. Kerbaol, B. Chapron, and P. W. Vachon, "Analysis of ERS-1/2 synthetic aperture radar wave mode images," *J. Geophys. Res., Oceans*, vol. 103, no. C4, pp. 7833–7846, 1998.
- [8] S. Hasselmann, C. Brüning, K. Hasselmann, and P. Heimbach, "An improved algorithm for the retrieval of ocean wave spectra from SAR image spectra," *J. Geophys. Res.*, vol. 101, no. C7, pp. 16 615–16 629, Jul. 1996.
- [9] G. Engen and H. Johnson, "SAR-ocean wave inversion using image cross spectra," *IEEE Trans. Geosci. Remote Sens.*, vol. 33, no. 4, pp. 1047–1056, Jul. 1995.
- [10] C. Mastenbroek and C. d. Valk, "A semi-parametric algorithm to retrieve ocean wave spectra from synthetic aperture radar," *J. Geophys. Res.*, vol. 105, no. C2, pp. 3497–3516, 1998.
- [11] J. S.-Stellenfleh, S. Lehner, and D. Hoja, "A parametric scheme for the retrieval of two-dimensional ocean wave spectra from synthetic aperture radar look cross spectra," *J. Geophys. Res.*, vol. 110, 2005, Art. no. C05 004.
- [12] S. Jian and G. Changlong, "Parameterized first-guess spectrum method for retrieving directional spectrum of swell-dominated waves and huge waves from SAR images," *J. Oceanology Limnology*, vol. 24, no. 1, pp. 12–20, Mar. 2006.
- [13] F. S. Pramudya, J. Pan, and A. T. Devlin, "Estimation of significant wave height of near-range traveling ocean waves using Sentinel-1 SAR images," *IEEE J. Sel. Topics Appl. Earth Observ. Remote Sens.*, vol. 12, no. 4, pp. 1067–1075, Apr. 2019.
- [14] J. S.-Stellenfleh, T. König, and S. Lehner, "An empirical approach for the retrieval of integral ocean wave parameters from synthetic aperture radar data," *J. Geophys. Res.*, vol. 112, no. C3, 2007, Art. no. C03019.
- [15] M. Li, S. Lehner, and T. Bruns, "Ocean wave integral parameters measurements using Envisat ASAR wave mode data," *IEEE Trans. Geosci. Remote Sens.*, vol. 49, no. 1, pp. 155–174, Jan. 2011.
- [16] J. E. Stopa and A. Mouche, "Significant wave heights from Sentinel-1 SAR: Validation and applications," *J. Geophys. Res., Oceans*, vol. 122, no. 3, pp. 1827–1848, 2017.
- [17] M. J. Collins, M. Ma, and M. Dabboo, "On the effect of polarization and incidence angle on the estimation of significant wave height from SAR data," *IEEE Trans. Geosci. Remote Sens.*, vol. 57, no. 7, pp. 4529–4543, Jul. 2019.
- [18] H. Wang, J. Zhu, J. Yang, and C. Shi, "A semiempirical algorithm for SAR wave height retrieval and its validation using Envisat ASAR wave mode data," *Acta Oceanologica Sinica*, vol. 31, no. 3, pp. 59–66, 2012.
- [19] L. Ren, J. Yang, G. Zheng, and J. Wang, "Significant wave height estimation using azimuth cutoff of C-band RADARSAT-2 single-polarization SAR images," *Acta Oceanologica Sinica*, vol. 34, no. 12, pp. 93–101, 2015.
- [20] G. Grieco, W. Lin, M. Migliaccio, F. Nirchio, and M. Portabella, "Dependency of the Sentinel-1 azimuth wavelength cut-off on significant wave height and wind speed," *Int. J. Remote Sens.*, vol. 37, no. 21, pp. 5086–5104, 2016.
- [21] H. Wang et al., "Empirical algorithm for significant wave height retrieval from wave mode data provided by the chinese satellite Gaofen-3," *Remote Sens.*, vol. 10, no. 3, 2018, Art. no. 363.
- [22] F. S. Pramudya, J. Pan, A. T. Devlin, and H. Lin, "Enhanced estimation of significant wave height with dual-polarization sentinel-1 SAR imagery," *Remote Sens.*, vol. 13, no. 1, pp. 124–141, 2021.
- [23] L. Bao et al., "Impact of polarization basis on wind and wave parameters estimation using the azimuth cutoff from GF-3 SAR imagery," *IEEE Trans. Geosci. Remote Sens.*, vol. 60, 2022, Art. no. 5234716.
- [24] W. Shao et al., "Wave retrieval under typhoon conditions using a machine learning method applied to Gaofen-3 SAR imagery," *Can. J. Remote Sens.*, vol. 45, no. 6, pp. 723–732, 2019.
- [25] C. Fan, T. Song, Q. Yan, J. Meng, Y. Wu, and J. Zhang, "Evaluation of multi-incidence angle polarimetric Gaofen-3 SAR wave mode data for significant wave height retrieval," *Remote Sens.*, vol. 14, no. 21, pp. 1–19, 2022.
- [26] T. Song, Q. Yan, C. Fan, J. Meng, Y. Wu, and J. Zhang, "Significant wave height retrieval using XGBoost from polarimetric Gaofen-3 SAR and feature importance analysis," *Remote Sens.*, vol. 15, no. 1, pp. 1–23, 2023.
- [27] S. Xue, X. Geng, X. H. Yan, T. Xie, and Q. Yu, "Significant wave height retrieval from Sentinel-1 SAR imagery by convolutional neural network," *J. Oceanogr.*, vol. 76, no. 6, pp. 465–477, 2020.
- [28] B. Quach, Y. Glaser, J. E. Stopa, A. A. Mouche, and P. Sadowski, "Deep learning for predicting significant wave height from synthetic aperture radar," *IEEE Trans. Geosci. Remote Sens.*, vol. 59, no. 3, pp. 1859–1867, Mar. 2021.
- [29] H. Wang et al., "Quad-polarimetric SAR sea state retrieval algorithm from Chinese Gaofen-3 wave mode images via deep learning," *Remote Sens. Environ.*, vol. 273, no. 112969, pp. 1–15, 2022.
- [30] W. Shao et al., "Sea state parameters retrieval from cross-polarization Gaofen-3 SAR data," *Adv. Space Res.*, vol. 65, no. 3, pp. 1025–1034, 2020.
- [31] W. Alpers, U. Pahl, and G. Gross, "Katabatic wind fields in coastal areas studied by ERS-1 synthetic aperture radar imagery and numerical modelling," *J. Geophys. Res.*, vol. 103, no. C4, pp. 7875–7887, Apr. 1998.
- [32] J. Horstmann, H. Schiller, J. S.-Stellenfleh, and S. Lehner, "Global wind speed retrieval from SAR," *IEEE Trans. Geosci. Remote Sens.*, vol. 41, no. 10, pp. 2277–2286, Oct. 2003.
- [33] N. Radkani and B. G. Zakeri, "Southern Caspian Sea wind speed retrieval from C-band Sentinel-1 A SAR images," *Int. J. Remote Sens.*, vol. 41, no. 9, pp. 3511–3534, May 2020.
- [34] W. Z. Shao, F. Nunziata, Y. G. Zhang, V. Corcione, and M. Migliaccio, "Wind speed retrieval from the Gaofen-3 synthetic aperture radar for VV and HH-polarization using a re-tuned algorithm," *Eur. J. Remote Sens.*, vol. 54, no. 1, pp. 318–337, Jan. 2023.
- [35] A. A. Mouche, D. Hauser, J.-F. Daloze, and C. Guerin, "Dual-polarisation measurements at C-band over the ocean: Results from airborne radar observations and comparison with ENVISAT ASAR data," *IEEE Trans. Geosci. Remote Sens.*, vol. 43, no. 4, pp. 753–769, Apr. 2005.
- [36] M. Portabella, A. Stoffelen, and J. A. Johannessen, "Toward an optimal inversion method for synthetic aperture radar wind retrieval," *J. Geophys. Res.*, vol. 107, no. C8, pp. 1-1–1-13, 2002.
- [37] D. E. Fernandez, J. Carswell, S. Frasier, P. Chang, P. Black, and F. Marks, "Dual-polarized C- and Ku-band ocean backscatter response to hurricane force winds," *J. Geophys. Res. Oceans*, vol. 111, no. C8, pp. 1–17, 2006.
- [38] X.-M. Li, T. Qin, and K. Wu, "Retrieval of sea surface wind speed from spaceborne SAR over the Arctic marginal ice zone with a neural network," *Remote Sens.*, vol. 12, no. 20, 2020, Art. no. 3291.
- [39] P. A. Hwang et al., "Cross-polarization geophysical model function for C-band radar backscattering from the ocean surface and wind speed retrieval," *J. Geophys. Res. Oceans*, vol. 120, no. 2, pp. 893–909, 2015.
- [40] G. Zhang, X. Li, W. Perrie, P. A. Hwang, B. Zhang, and X. Yang, "A hurricane wind speed retrieval model for C-band RADARSAT-2 cross-polarization ScanSAR images," *IEEE Trans. Geosci. Remote Sens.*, vol. 55, no. 8, pp. 4766–4774, Aug. 2017.
- [41] A. A. Mouche, B. Chapron, B. Zhang, and R. Husson, "Combined co and cross-polarized SAR measurements under extreme wind conditions," *IEEE Trans. Geosci. Remote Sens.*, vol. 55, no. 12, pp. 6746–6755, Dec. 2017.
- [42] T. Song, C. Fan, Q. Yan, and J. Zhang, "Dependence of the azimuth cutoff from quad-polarization Gaofen-3 SAR image on significant wave height and wind speed," in *Proc. IEEE Int. Geosci. Remote Sens. Symp.*, 2022, pp. 2299–2302.
- [43] V. Corcione, G. Grieco, M. Portabella, F. Nunziata, and M. Migliaccio, "A novel azimuth cutoff implementation to retrieve sea surface wind speed from SAR imagery," *IEEE Trans. Geosci. Remote Sens.*, vol. 57, no. 6, pp. 3331–3340, Jun. 2019.
- [44] H. Li, A. Mouche, H. Wang, J. E. Stopa, and B. Chapron, "Polarization dependence of azimuth cutoff from quad-pol SAR images," *IEEE Trans. Geosci. Remote Sens.*, vol. 57, no. 12, pp. 9878–9887, Dec. 2019.
- [45] Q. Zhang, "System design and key technologies of the GF-3 satellite," *Acta Geodaetica Cartographica Sinica*, vol. 46, no. 3, pp. 269–277, 2017.
- [46] J. S.-Stellenfleh and S. Lehner, "Measurement of 2-D sea surface elevation fields using complex synthetic aperture radar data," *IEEE Trans. Geosci. Remote Sens.*, vol. 42, no. 6, pp. 1149–1160, Jun. 2004.
- [47] F. Fois, P. Hoogeboom, F. L. Chevalier, and A. Stofflen, "Future ocean scatterometry: On the use of cross-polar scattering to observe very high winds," *IEEE Trans. Geosci. Remote Sens.*, vol. 43, no. 9, pp. 5009–5020, Sep. 2015.
- [48] M. B. Rivas and A. Stoffelen, "Characterizing ERA-Interim and ERA5 surface wind biases using ASCAT," *Ocean Sci.*, vol. 15, pp. 831–852, 2019.
- [49] R. Zhai et al., "Applicability evaluation of ERA5 wind and wave reanalysis data in the South China Sea," *J. Oceanology Limnology*, vol. 41, no. 2, pp. 495–517, Mar. 2023.

- [50] B. Zhang, W. Perrie, and Y. He, "Validation of RADARSAT-2 fully polarimetric SAR measurements of ocean surface waves," *J. Geophys. Res. Oceans*, vol. 115, no. C6, pp. 1–11, 2010.
- [51] X. Chu, Y. He, and G. Chen, "Asymmetry and anisotropy of microwave backscatter at low incidence angles," *IEEE Trans. Geosci. Remote Sens.*, vol. 50, no. 10, pp. 4014–4024, Oct. 2012.
- [52] V. N. Kudryavtsev, S. Fan, B. Zhang, A. A. Mouche, and B. Chapron, "On quad-polarized SAR measurements of the ocean surface," *IEEE Trans. Geosci. Remote Sens.*, vol. 57, no. 11, pp. 8362–8370, Nov. 2019.
- [53] B. Zhang and W. Perrie, "Recent progress on high wind-speed retrieval from multi-polarization SAR imagery: A review," *Int. J. Remote Sens.*, vol. 35, no. 11/12, pp. 4031–4045, Jun. 2014.
- [54] V. Kudryavtsev, I. Kozlov, B. Chapron, and J. A. Johannessen, "Quad polarization SAR features of ocean currents," *J. Geophys. Res., Oceans*, vol. 119, no. 9, pp. 6046–6065, 2014.
- [55] C. R. d. Macedo, J. C. B. d. Silva, A. Buono, and M. Migliaccio, "Multi-polarization radar backscatter signatures of internal waves at L. band," *Int. J. Remote Sens.*, vol. 43, no. 6, pp. 1943–1959, 2022.
- [56] R. C. Beal, D. G. Tilley, and F. M. Monaldo, "Large- and small-scale spatial evolution of digitally processed ocean wave spectra from seasat synthetic aperture radar," *J. Geophys. Res. Oceans*, vol. 88, no. C3, pp. 1761–1778, 1983.
- [57] Y. X. Sheng et al., "Validation of significant wave height retrieval from co-polarization Chinese Gaofen-3 SAR imagery using an improved algorithm," *Acta Oceanologica Sinica*, vol. 37, no. 6, pp. 1–10, Jun. 2018.
- [58] S. B.-Belhouari and A. Bermak, "Gaussian process for nonstationary time series prediction," *Comput. Statist. Data Anal.*, vol. 47, no. 4, pp. 705–712, Nov. 2004.
- [59] W. Shao, Y. Sheng, and J. Sun, "Preliminary assessment of wind and wave retrieval from Chinese Gaofen-3 SAR imagery," *Sensors*, vol. 17, no. 8, Jul. 2017, Art. no. 1705.
- [60] W. Shao et al., "An empirical algorithm to retrieve significant wave height from sentinel-1 synthetic aperture radar imagery collected under cyclonic conditions," *Remote Sens.*, vol. 10, no. 9, Aug. 2018, Art. no. 1367.
- [61] W. Shao, Z. Lai, F. Nunziata, A. Buono, X. Jiang, and J. Zuo, "Wind field retrieval with rain correction from dual-polarized Sentinel-1 SAR imagery collected during tropical cyclones," *Remote Sens.*, vol. 14, no. 19, Oct. 2022, Art. no. 5006.



Chenqing Fan received the M.S. degree in signal and information processing from the China University of Petroleum (East China), Qingdao, China, in 2009. He is currently an Associate Research Professor with the First Institute of Oceanography, Ministry of Natural Resources, Qingdao. His research interests include radar altimeter, microwave radar imaging, and ocean remote sensing.



Junmin Meng received the Ph.D. degree in physical oceanography from the Ocean University of China, Qingdao, China, in 2002. He is now a Research Professor with the First Institute of Oceanography, Ministry of Natural Resource, Qingdao. His research interests include ocean internal wave and synthetic aperture radar (SAR) marine applications.



Jie Zhang received the Ph.D. degree in applied mathematics from Tsinghua University, Beijing, China, in 1993. He is currently the Dean with the College of Oceanography and Space Informatics, China University of Petroleum (East China), Qingdao, China, and also a Professor with the First Institute of Oceanography, Ministry of Natural Resources, Qingdao. His research interests include remote sensing and oceanography.



Tianran Song received the M.S. degree in intelligent information processing from the China University of Petroleum (East China), Qingdao, China, in 2023. She is currently an Electrical Engineer with Goertek, Weifang, China. Her research interests include ocean wave observations and synthetic aperture radar (SAR) marine applications.



Weifu Sun received the Ph.D. degree in marine environmental science from the Ocean University of China, Qingdao, China, in 2016. He is currently an Associate Research Professor with the First Institute of Oceanography, Ministry of Natural Resources, Qingdao, China. His research interests include the sea surface parameters retrieval and products applications based on the satellite remote sensing.



Zhichao Zheng received the B.S. degree in software engineering from the Minzu University of China, Beijing, China, in 2022. He is currently working toward the M.S. degree in communications engineering with the China University of Petroleum, Qingdao, China. His research interests include microwave remote sensing of ocean waves, wave parameters retrieval, and wave spectrum retrieval.



Qiushuang Yan received the Ph.D. degree in oceanographic detection technology from the Ocean University of China, Qingdao, China, in 2018. She is currently with the School of Oceanography and Spatial Information, China University of Petroleum (East China), Qingdao. Her research interests include the ocean microwave remote sensing mechanisms and methods for detecting wind, waves, and currents.